Characterizing the Morphology of Solvent Annealed PCBM/P3HT Bilayers using GIXRD and Raman Spectroscopy

A Thesis Presented for the
Master of Science
Degree
The University of Tennessee, Knoxville

Tyler Evan McPherson
May 2014

Copyright © 2014 by Tyler Evan McPherson
All rights reserved.

ACKNOWLEDGEMENTS

I would like to acknowledge and thank my advisor Dr. Mark Dadmun for his knowledge, guidance, and patience throughout my time at the University of Tennessee, Knoxville. I will be forever thankful for the research experience and knowledge I have gained while working in his lab. I would like to thank Dr. Jon Camden and his graduate students, especially Hobbie Turley, for allowing me time on their Raman spectrometer and also hours spent setting up the instrument for my experiments. I would also like to thank Dr. Joseph E. Spruiell for training and assistance in GIXRD experiments.

Secondly, I would like to thank my parents, Randal and Kathy McPherson, and my siblings Jessica and Wesley. Without your support, I would not be where I am today. You have always pushed me to do my best and achieve whatever I set my mind to. I hope to continue to make you proud. I would also like to thank my girlfriend, Kim McLendon. Thank you for your unwavering love and support as I reached for my goals.

Lastly, I would like to acknowledge my friends and lab mates. From the insightful conversations about my research to the fun times we had, you have made my experience enjoyable. I truly believe I have made not only connections for the future, but friends as well. I will truly miss each and every one of you.

ABSTRACT

A growing demand for new forms of renewable energy has been at the forefront of scientific research. Organic photovoltaics (OPVs) provide a promising alternative to the expensive inorganic solar cells used today. Poly(3-hexylthiophene) (P3HT) and [6,6]-phenyl C61-butyric acid methyl ester (PCBM) are common donor and acceptor materials used in the active layer of an OPV device. These systems have reached power conversion efficiencies of approximately 12 %. However, little is known about the actual morphology. A better understanding of the morphology would allow researchers to optimize device fabrication to increase the device performance. As-cast devices are limited by the processing conditions which they were casted. Post-annealing allows us to alter these samples. Unlike thermal annealing, solvent annealing provides a slow, selective way to alter the samples. We looked to explore how solvent annealing affects a P3HT:PCBM bilayer. By increasing the loading of PCBM, we are able to investigate different morphologies based on the miscibility of the system. Grazing Incidence X-ray Diffraction (GIXRD), Raman spectroscopy, and Near-Edge X-ray Absorption of Fine Structure (NEXAFS) were used to explore the morphology of these systems.

TABLE OF CONTENTS

CHAPTER I Introduction 1
1.1 Solar Energy 1
1.2 Inorganic Solar Cells 1
1.3 Organic Photovoltaics 3
1.4 Charge Generation and Transfer 6
1.5 Power Conversion Efficiency 8
1.6 Architecture and Morphology 9
1.7 Post Annealing Processes 13
1.8 Goals and Overview 16
CHAPTER II Correlating aggregation as determined by Raman spectroscopy and Crystallinity 18
2.1 Raman Spectroscopy 18
2.2 Grazing Incidence X-ray Diffraction (GIXRD) 23
2.3 Experimental Methods 25
2.3.1 Sample Preparation 25
2.3.2 Spin Coating 26
2.3.3 Solvent Annealing 28
2.3.4 Raman Spectrometry 29
2.3.5 GIXRD 31
2.4 Results and Discussion 31
2.4.1 Correlating Raman “Aggregation” and Crystallinity 31
2.4.2 Impact of Wavelength Choice on Measured Percent Aggregation 40
CHAPTER III Near edge x-ray absorption of fine structures 42
3.1 Experimental Methods 45
3.2 Results and Discussion 47
3.2.1 NEXAFS on Thermally annealed Bilayer samples 47
3.2.2NEXAFS of P3HT:PCBM Solvent annealed Mixed Layers and Thermally annealed true Bilayers 58
CHAPTER IV Physical properties of thin Polymer films 62
4.1 Young's Modulus 62
4.2 Determining Diffusion Coefficients of Gases in Polymer Thin Films 64
4.3 Experimental Methods 66
4.3.1 Preparation of polystyrene thin films 66
4.3.2 Ellipsometry 67
4.4 Results and Discussion 68
4.4.1 Determining Young's Modulus of thin polymer films 68
4.4.2 Determining the Diffusion Coefficients of Gases through Thin Polymer Films 71
CHAPTER VII Conclusion and future work 80
REFERENCES 84
APPENDIX 93
VITA 100

LIST OF TABLES

Table 2.3.1: Spin coating processing parameters and film thicknesses of 10/90, 20/80, 40/60 PCBM:P3HT bilayer samples. 28
Table 3.4.1: Percentage of P3HT in a 1/0.8 P3HT:PCBM mixed layer sample solvent annealed in CS_2 at 50 % or 90 % SVP 59
Table 3.4.2: Percentage of P3HT in thermally annealed PCBM:P3HT bilayers with a loading of 11 % PCBMCBM, 30 % PCBM, and 37 % PCBM 61
Table 4.4.1: Parameters used to determine the elastic modulus. 69

LIST OF FIGURES

Figure 1.2.1:Power efficiencies of different solar cells from 1976 to 2010 [2]..... 2
Figure 1.3.1:Cross-sectional view of typical OPV components [11]. 4
Figure 1.3.2:Common structures of donor and acceptor polymers used in active layer of OPVs [16]. 6
Figure 1.5.1:The charge transfer process of OPVs occurs when 1) photon of sunlight excites an electron-hole pair known as an exciton 2) exciton diffused to the donor/acceptor interface 3) Once the exciton reaches the interface, paired charges separate and transfer to their respective electrode. 7
Figure 1.6.1: Head-to-tail and Head-to-head sequencing of P3HT. The substituent R represents the hexyl alkyl side-chain. 11
Figure 1.6.2: Representation of local structure morphology of PCBM:P3HT blends in a BHJ [33]. Straight lines indicate crystalline P3HT. Curved lines represent the amorphous region a mixture of P3HT. 12
Figure 2.1.1: Raman spectra (C-C and C=C peaks) non-annealed and annealed regioregular P3HT:PCBM blends using a (a) 633 nm (b) 488 nm excitation wavelength [48]. A shift in peak position and FWHM is noticed at 488 nm, ... 19
Figure 2.1.2 : Raman spectra of the P3HT C=C symmetric mode at 1450 cm^{-1}. The peak actually consists of two distinct peaks, an aggregated species at 1445 cm^{-1} and a unaggregated species at 1470 cm^{-1} [49].
Figure 2.2.1: Illustration of orientation of A) Edge-on B) Face-on P3HT chains. 24
Figure 2.2.2: GIXRD spectra of P3HT 24
Figure 2.3.1: Illustration of spin coating process..... 27
Figure 2.3.2: Schematic diagram of solvent annealing apparatus where a) sample is lowered into the column filled with ODCB vapor b) sample is set 90 cm down the column equivalent to 90% SVP [57]. 29
Figure 2.3.3: Diagram of the Raman Setup [58]..... 30
Figure 2.4.2 :Area of the P3HT crystalline peak of 10/90, 20/80, and 40/60 PCBM/P3HT bilayers solvent annealed for 30,60, and 90 minutes in ODCB at a SVP of 90%. ... 32
Figure 2.4.3: Average crystal size of 10/90, 20/80, 40/60 PCBM/P3HT bilayer samples solvent annealed in ODCB for 0, 30, 60, and 90 minutes. 34
Figure 2.4.4: Percent aggregation of P3HT in 10/90,20/80, 40/60 PCBM/P3HT bilayer samples solvent annealed for 0, 30, 60, and 90 minutes in ODCB at a SVP of 90%. 35
Figure 2.4.5: Illustration of three types of ordering of P3HT. 38
Figure 2.4.6: Surface area of 10/90, 20/80, and 40/60 PCBM/P3HT bilayer samples. Surface area refers to not only the crystals but also the regions which are not crystalline or amorphous. 39
Figure 2.4.7: Percent aggregation of 20/80 PCBM:P3HT bilayer solvent annealed for 0,30,60, and 90 minutes in ODCB at 90 % SVP. The resulting percent aggregation was obtained by an excitation wavelength of 472, 514, and 532 nm. 41
Figure 3.1.1: Illustration of how NEXAFS spectra are produced. Soft x-rays excite core shell electrons to unfilled anti-bonding molecular orbitals. The energy difference

between the core level and excited energy levels produce a spectra. Key features of fullerene/thiophene OPVs are the π* and σ* transitions [60]..... 42
Figure 3.1.2: Schematic illustration of NEXAFS [36]. The sample is tilted at an incidence angle θ. Data was taken for five different incidence angles of 20°,44°,55°,70°, and 80°..... 46
Figure 3.2: Illustration of sample preparation and annealing process. 47
Figure 3.2.1: NEXAFS spectra for 20/80 PCBM:P3HT bilayer sample. P3HT layer was thermally annealed at 150°C for 15 minutes before entire sample was thermally annealed at 150 °C for A) 0 B) 20 and C) 60 minutes. Each spectra was taken at incident angles of 20,44,55,70, and 80 degrees. 47
Figure 3.2.2: Percent of P3HT of 20/80 PCBM:P3HT bilayer..... 49
Figure 3.2.3: NEXAFS spectra of 20/80 bilayer annealed samples. The P3HT layer was first thermally annealed for A) 0 B) 20 C) 60 minutes. After depositing the PCBM on top of the preheated P3HT layer, the entire sample was annealed for 15 minutes. 50
Figure 3.2.4: Percent of P3HT in a 20/80 PCBM:P3HT annealed bilayer at the top12 nm (-50 V bias), top 9 nm (-150 V), and top 2 nm (-225 V) from the surface of the film. 52
Figure 3.2.5: NEXAFS spectra of 40/60 PCBM:P3HT bilayer as-cast samples. P3HT layer was annealed for A) 0 B) 20 and C) 60 minutes prior to deposition of PCBM layer..... 53
Figure 3.2.6: Percentage of P3HT of 40/60 bilayer as-cast sample at three different biases of -50, -150, and -225 V..... 54
Figure 3.2.7: NEXAFS spectra of 40/60 pre-annealed bilayer. Each sample was annealed 55
Figure 3.2.8: Percentage of P3HT of 40/60 bilayer annealed samples at 50 V (top 1-2 nm), 150 V (top 9 nm), and 225 V (top 12 nm)..... 56
Figure 4.1: Graph plotting the length of the wrinkles (L) as a function of the variable $ah^{1/2}$ [65]..... 63
Figure 4.2.1: A timeline of the diffusion of a gas through a thin film of polystyrene..... 64
Figure 4.2.2: A typical curve for the amount of diffused gas (Qt) versus time graph [65]. θ is determined by the linear best fit line..... 65
Figure 4.3.1: Illustration of Ellipsometer apparatus. 67
Figure 4.4.1: Wrinkling of a thin film of polystyrene by placing a droplet of water on top of a film in an aqueous environment..... 69
Figure 4.4.2: Graph relating the number of wrinkles (N) as a function of the radius of the droplet and thickness of the film [65]..... 70
Figure 4.4.1: Graph of volume of air diffused (mL) as a function of time (sec)..... 73
Figure 4.4.2: Graph of volume of oxygen diffused as a function of time..... 74
Figure 4.4.3: Graph of volume of N_2 gas diffused as a function of time..... 75
Figure4.4.4: Graph of diffusion of argon gas as a function of time..... 76
Figure 4.4.5: Illustration of transport of gas molecules across a membrane [72]..... 78
Figure 2.4.1: GIXRD spectra of A) 10/90 PCBM:P3HT Bilayer B) 20/80 PCBM:P3HT bilayer C) 40/60 PCBM:P3HT bilayer. All three systems were solvent annealed in ODCB at 90 percent SVP for 30,60, and 90 minutes. 94

Figure 1A: Linear fit of volume of oxygen in air diffused as a function of time. 95
Figure 2A: Linear Fit of change in the volume of nitrogen in air as a function of time... 95
Figure 3A: Linear Fit of change in the volume of pure oxygen as a function of time 96
Figure 4A: Linear fit of volume change of pure nitrogen through 108.17 nm polystyrene film. 97
Figure 5A: Linear fit of volume change of pure nitrogen through a 107.47 nm polystyrene film. 98
Figure 6A: Volume change of argon gas as a function of time. A linear fit was used to calculate the x intercept (time lag θ). 99

CHAPTER I
INTRODUCTION

1.1 Solar Energy

From the cars we drive to the lights in our homes, energy is an important aspect of the world we live in today. Research predicts that the world's energy consumption will increase 44% from 2006 to 2030 [1]. Eventually, non-renewable resources such as petroleum, coal, and other fossil fuels, which currently produce the majority of the energy used, will be completely consumed. Therefore, both academia and industry have increased research in renewable forms of energy, where one of the promising renewable resources is solar energy.

Every hour, enough solar energy is produced by the sun to satisfy the energy needs of the entire planet for a year [2]. With this abundant source of energy, one would expect a large contribution of solar energy to the world's energy supply. Yet, only one tenth of one percent of our energy supply is from solar energy [2,3]. Why is such a vast amount of energy not being utilized? To address this question, it is first important to explore the current devices used to harvest solar energy.

1.2 Inorganic Solar Cells

Inorganic solar cells made from Silicon (Si) based materials constitute 90 percent of the total solar energy market today[2]. Spurred by the semi-conductor industry in the 1950s, the knowledge and production methods of Si-based materials were already well-established and led to an easy transition of the use of these materials in solar energy. By

the 1970's, Si-based solar cells became the leading devices in the solar energy industry. However, these devices have many shortcomings. First, the recent shortage of silicon and production cost has dramatically increased the cost to consumers. With the increase in cost, 4-8 years of use is required before the economic benefits of installing these devices are seen [4]. To combat this problem, devices need to have improved longevity and/or higher efficiencies. However, Si inorganic solar cells are brittle and require a rigid support, both limiting the lifetime of the solar cell.

Figure 1.2.1 shown below illustrates recent trends in the power conversion efficiencies of different types of solar cells. Although inorganic solar cells have reached power efficiencies as high as 40 percent, only marginal improvements have been obtained in recent years [5]. One area of focus for recent research is using polymers to provide a cheaper alternative to the inorganic solar cells.

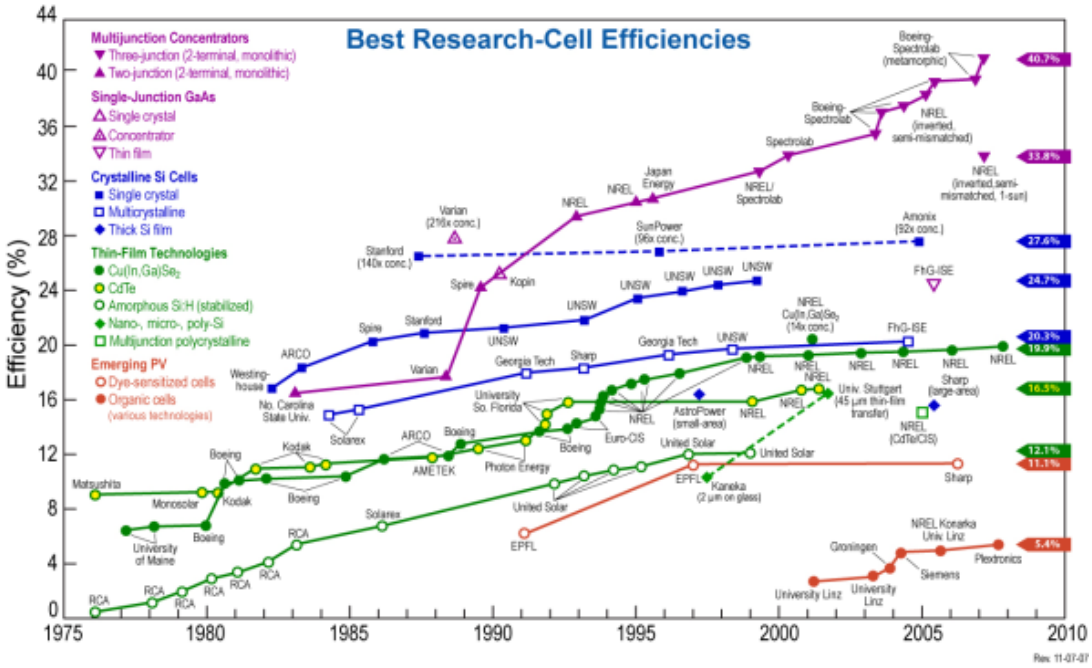

Figure 1.2.1: Power efficiencies of different solar cells from 1976 to 2010 [2].

1.3 Organic Photovoltaics

Polymer-based organic photovoltaics (OPVs) are promising devices capable of competing with inorganic solar cells. Unlike Si-based devices, polymer-based OPVs are not limited to a rigid support. Any transparent, stable substrate, such as thin plastic sheets, could be used as an inexpensive flexible support. The molecular structure of the polymer can also be readily modified to address the specific needs of devices. Since polymers can be functionalized to increase solubility, roll-to-roll ink printing of the active layer components already presents a cheap method to manufacture the cells [6]. Theoretical studies have shown possible power conversion efficiency (PCE) well above 18% [7]. Although power conversion efficiencies in the laboratory are already at 12 %, little is known about the actual morphology [7]. A better understanding of the morphology of the active layer would allow researchers to more readily optimize OPVs to create higher power efficiency devices.

Before discussing how the device works, it is first important to take a closer look at the components of an OPV. A cross sectional view of a typical organic solar cell is shown in Figure 1.3.1. A transparent substrate is used as the solid support of the device. Since sunlight must pass through this layer, typical materials such as glass or transparent plastics are used due to their transparency and low cost benefits. The next layer consists of a conducting oxide layer, usually indium tin oxide (ITO). This layer acts as the anode to the cell allowing current to flow out of the cell. Other alternatives such as carbon nanotubes [8], highly-conducting polymers [9], and graphene [10] have all been studied to replace the ITO conducting layer.

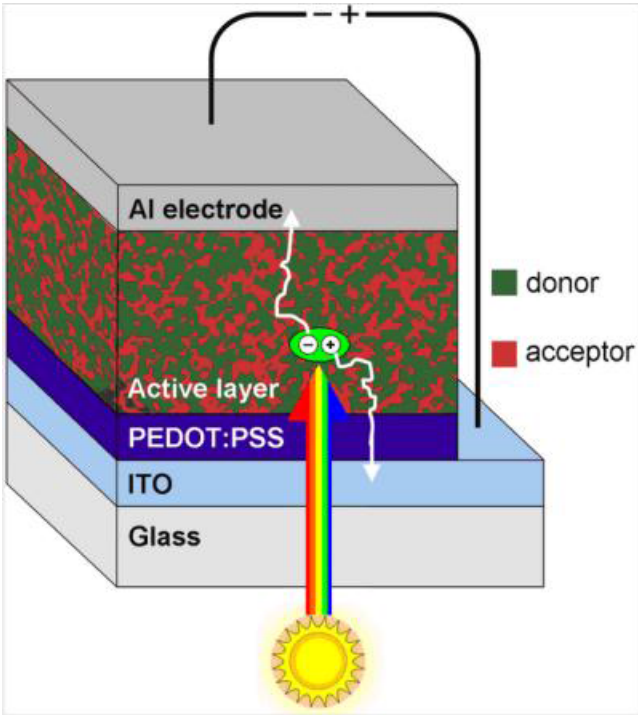

Figure 1.3.1:Cross-sectional view of typical OPV components [11].

A hole transport layer is placed on top of the ITO glass to allow holes to be transferred through the layer but block electrons which may short the circuit. This layer also acts as an optical filter, optimizing the absorbance of the active layer. A typical material used as this hole transport layer is poly(3,4-ethylenedioxythiophene):poly(styrene-sulfonate),which is commonly called PEDOT:PSS. Interactions between this hole transport layer and the components in the active layer have been shown to cause a decrease in efficiency or even failure of the devices [12]. Intense research has been conducted to limit the interactions between the PEDOT:PSS and active layer of the devices [9].

The next layer on the device is the active layer. Charge creation, separation, and charge transfer all occur in the active layer making it the most important contributor to device performance. Conjugated thiophene/fullerene based organic solar cells have been intensely studied for use in the active layer. Figure 1.3.2 shows common donor and acceptor materials used to fabricate the active layer. By utilizing the delocalized π-electrons, conjugated thiophene/fullerene OPVs are able to absorb sunlight, excite electrons and realize charge transport through the system. Poly(3-hexylthiophene) (P3HT) is a typical donor material, which is used because it strongly absorbs in the visible spectrum [3]. Also, P3HT is a semi-crystalline polymer leading to a high degree of intermolecular order and high hole mobility [13]. 1-(3-methyloxycarbonyl) propyl (1-phenyl [6, 6] C61 (PCBM) is used as an acceptor material capable of stabilizing charges and is readily dissolved in numerous solvents. By accepting up to 6 electrons, PCBM is an excellent material to transport charges throughout the active layer.

The last component to complete the circuit is the cathode. An ideal cathode needs to be highly conductive with minimal chemical and physical interaction between it and the active layer[14]. The cathode is usually composed of a thin substrate with a low work function such as aluminum. However, interactions still occur between the aluminum and active layer, limiting device performance. To combat this problem, materials such as calcium [14], and LiF [15] have also been studied to provide a cushion between the layers. Finally, a protective layer of glass or plastic is placed on top of the cathode to insure moisture cannot penetrate into the device.

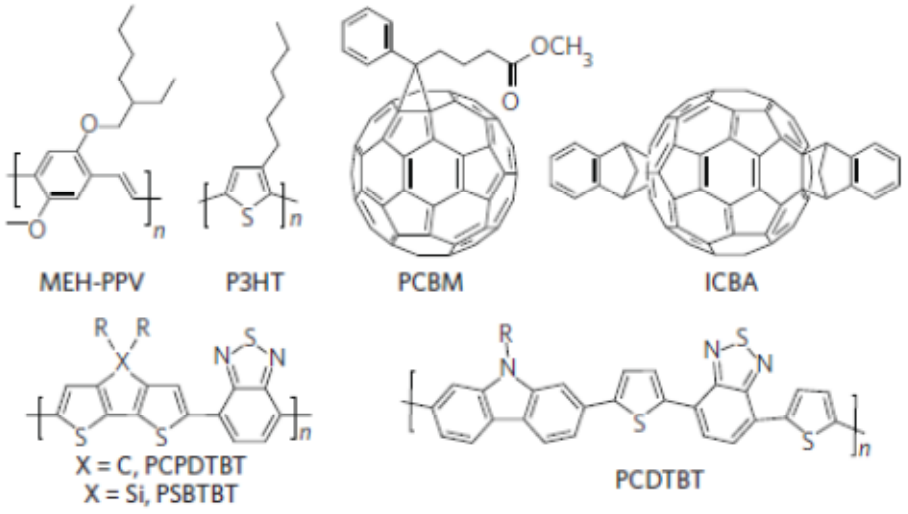

Figure 1.3.2:Common structures of donor and acceptor polymers used in active layer of OPVs [16].

1.4 Charge Generation and Transfer

The mechanisms to generate and transport charges in organic solar cells is shown in Figure 1.4.1. When sunlight enters the active layer of the device, the polymer absorbs the photons, which can excite electrons from their highest-occupied molecular orbital (HOMO) to the lowest-unoccupied molecular orbital (LUMO). Unlike the p-n junction of inorganic semiconductors where free charge carriers quickly separate, OPV devices create an exciton, which is an electron-hole pair that is bound together by Coulombic attractions. The exciton then diffuses to the interface between the donor and acceptor material. Excitons are usually only able to diffuse between 10 to 20 nm before recombining [3, 17]. At the interface between the donor and accepter (D/A) materials, the exciton separates into free charges, allowing the individual charges to transport through the active layer until they reach their respective electrodes or recombine within the

system. Splitting the exciton into two separate charges takes approximately 0.1-0.4 eV [18]. This energy barrier cannot be overcome by simple thermal energy. Only an electron accepting material with a high electron affinity can separate excitons[3]. Since holes and electrons are in close proximity to each other, it is easy for them to recombine leading to lower power efficiencies. Thus, a crucial aspect in the production of electricity from solar energy within an organic photovoltaic is the morphology, which affects the diffusion of the exciton to the D/A interface, exciton dissociation and transport of free charges to the electrodes.

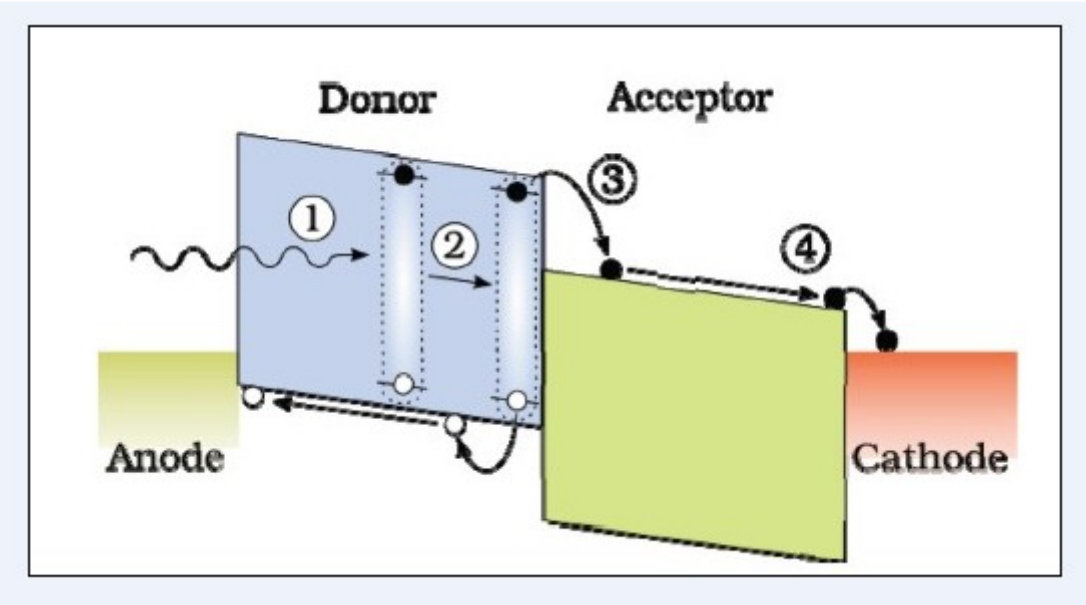

Figure 1.4.1:The charge transfer process of OPVs occurs when 1) photon of sunlight excites an electron-hole pair known as an exciton 2) exciton diffused to the donor/acceptor interface 3) Once the exciton reaches the interface, paired charges separate and transfer to their respective electrode.

1.5 Power Conversion Efficiency

Power conversion efficiency (PCE) is a term used to express how efficient a device is at converting solar energy into electricity. The PCE, η, of an OPV is determined by the equation:

$$\eta = V_{OC} \text{ x } J_{SC} \text{x FF} \quad (1.5.1)$$

The parameter V_{oc} is the open circuit voltage. The main factor that affects the value of V_{oc} is the difference between the HOMO of the donor material and the LUMO of the acceptor material [16]. Lowering the HOMO of the donor material and increasing the LUMO of the acceptor will lead to a greater value of V_{oc}. Most conjugated polymers have a band gap energy of greater than 2 eV, which corresponds to a wavelength of <600 nm [19]. An optimal band gap energy to absorb a broader range of the solar spectrum is <1.8 eV [16]. This is often achieved by designing new alternative donor and accepter materials. However, controlling the chain planarity and tuning the conjugation length are other methods to improve the V_{oc} [16].

Another factor to consider in determining the efficiency of the solar cell is the short-circuit current density, J_{sc}. The degree of domain separation, degree of crystallinity, and solubility of the donor and acceptor material are all important factors to consider when trying to improve the J_{sc} [16]. Each component of J_{sc} relates back to the morphology of the active layer. By optimizing each individual factor, a higher value of J_{sc} is obtainable. Although V_{oc} and J_{sc} can be improved, it is still a challenge to improve both factors simultaneously [20-23]. Fine tuning both parameters to reach an optimal performance is key to achieving an economical device.

Finally, the last component of the efficiency equation is the fill factor (FF). This is the ratio between the maximum power output and the product of J_{sc} and V_{oc}. Charge carrier mobility, interface recombination, series and shunt resistances, film morphology, and miscibility between the donor and acceptor all have been found to play a factor in determining the fill factor of a solar cell [24]. Gaining a better understanding of the FF is still an obstacle facing researchers. Out of the three parameters, the FF is the least understood [25]. However, improving both the V_{oc} and the J_{sc}, an increase in the fill factor will usually also occur.

1.6 Architecture and Morphology

The bulk heterojunction (BHJ) is by far the most studied architecture in recent years. With this architecture, a donor and an acceptor material are mixed together to form interwoven domains. Poly(1,4-phenylene vinylene) (PPV) was the first conjugated polymer researched in BHJ devices[26]. Power conversion efficiencies of poly(2-methoxy-5-{3',7'-dimethyloctyloxy]-p-phenylenevinylene (MDMO-PPV)/fullerene systems reached 3.0 % [26,27]. Even in the earliest systems, research revealed a strong correlation between morphology and device performance.

Understanding the morphology and how to alter it to improve device performance became a crucial area of research. This research addresses factors that contribute to changing the morphology. Differences in morphology caused by interactions between solvent molecules and the donor and/or acceptor materials were first investigated by Shaheen et. al. By examining a PPV:PCBM mixture dissolved in a variety of solvents,

they found that the choice of deposition solvent can limit large scale phase segregation, which improves the efficiency of the devices [28]. This confirmed that the choice of casting solvents impacts the final morphology. Hoppe et. al elaborated on this dependence by using high-resolution scanning electron microscopy to image MDMO-PPV:PCBM blends [29] cast from different solvents. Their findings showed that a blended layer processed from toluene creates large domains of PCBM aggregates than if cast from chlorobenzene, which limits charge transfer. As the concentration of PCBM increases, there was also an increase in the aggregation size [29]. They concluded that the choice of casting solvent affects the morphology of these devices. These early findings demonstrate how sensitive casting conditions are to the device performance.

However, PPV does not have the physical properties needed to create devices with targeted efficiencies. To improve the efficiencies of the devices, research has focused on conjugated polymers with improved absorption properties. Poly(3-alkylthiophene)s (P3AT)s quickly became the model polymers due to their promising attributes of solar device performance, including high field effect mobility, and semi-crystalline structure [30,31]. Poly(3-hexylthiophene) (P3HT) became a model polymer used in OPVs. By adding a hexyl side chain to the thiophene backbone, the solubility was improved, yet introduced a new problem.

When polymerizing P3HT, a head-to-head or head-to-tail sequence can occur. These two sequences are shown in Figure 1.6.1, where R represents the hexyl alkyl side-chain. The percent of head-to-tail or head-to-head connections along the backbone chain defines the regioregularity of the polymer. Research has explored how the regioregularity affects the crystallization and charge mobility of P3HT in OPVs. Sirringhaus et al.

reported a strong relationship between the molecular weight and regioregularity of the P3HT molecule to the molecular orientation and absorbance of light. Films with their side chains oriented normal to the substrate and polymer backbone in the plane of the substrate are referred to as having an edge-on conformation. Likewise, films with their polymer backbone and side chains normal to the substrate are known as face-on oriented. Using highly regioregular (>91%) P3HT rather than low regioregularity(86-90%) P3HT gives rise to the preferred edge-on conformation instead of a face-on conformation [32]. They concluded that the alkyl chain that is attached to the backbone causes steric hindrance between P3HT chains limiting π-π stacking between neighboring chains. The alkyl side-chains of the highly regioregular P3HT are oriented in the same direction, which allows for improved ordering of the P3HT chains enabling crystallization.

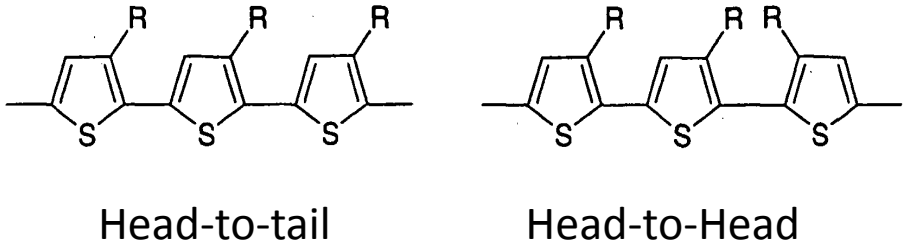

Figure 1.6.1: Head-to-tail and Head-to-head sequencing of P3HT. The substituent R represents the hexyl alkyl side-chain.

To control and predict the morphology of the BHJ systems, a better understanding of the interactions between donor and acceptor material is needed. PCBM is miscible in P3HT up to 22% [33].Based on small angle neutron scattering (SANS) results, our group proposed a novel morphology of the PCBM:P3HT bulk heterojunction. Figure 1.6.2

shows this proposed rivers and streams morphology. The illustration depicts PCBM as dark circles and straight lines as P3HT crystalline domains, while curved lines show amorphous regions of P3HT. As previously mentioned, both P3HT and PCBM form separate domains in the sample. Not only are there two separate domains, but also there is a third domain containing a homogenous mixture of both components.

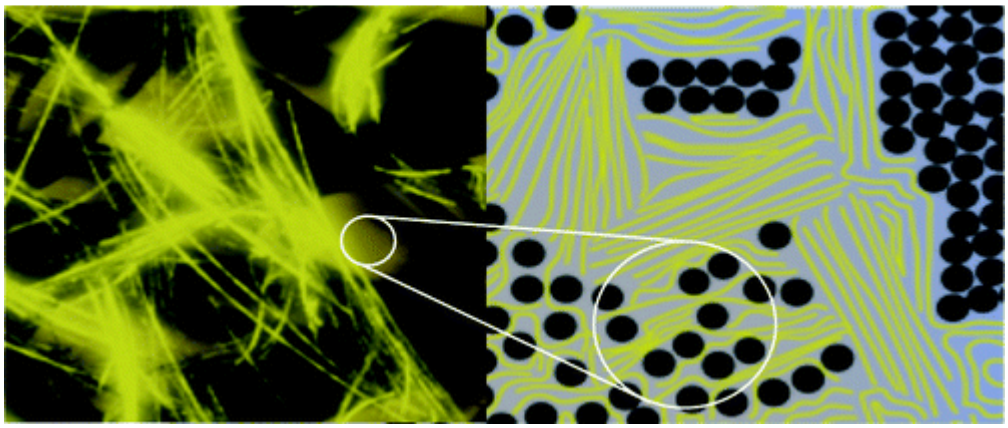

Figure 1.6.2: Representation of local structure morphology of PCBM:P3HT blends in a BHJ [33]. Straight lines indicate crystalline P3HT. Curved lines represent the amorphous region a mixture of P3HT.

Bulk heterojunction devices do have drawbacks. Although larger domains are beneficial for charge transport, if the distance of a domain is larger than 10 nm, an electron-hole pair can recombine [2,3,5,6]. If the distance is too great, excitons will recombine causing poor device performance. A discontinuous island of donor or acceptor material may also occur, limiting charge transport to the electrodes [34]. Solving these issues or creating a different morphology that combats these problems is essential to device improvements.

Bilayers provide a promising architecture with a defined pathway for charges to be collected. In this architecture, a layer of donor and acceptor materials are separately deposited on top of each other creating two separate layers. In thicker samples, the interfacial area between the two layers will consist of a homogenous mixture of donor/acceptor material. This architecture may allow a pathway with direct contact to the respective electrode, eliminating the problem of insufficient charge transfer. However, the morphology of this architecture is even less understood than the BHJ. Also, an increase in the interfacial area between the two separate layers will optimize exciton separation [35]. Post-annealing the sample is essential to create this greater interfacial area.

1.7 Post Annealing Processes

After the solvent evaporates from the active layer during deposition, the morphology of the active layer is kinetically "frozen". Thus, performance of as-cast devices is limited by the processing conditions [36, 37]. Altering the morphology after casting is essential to improve device efficiencies. Creating a greater interfacial area improves exciton dissociation, while potentially creating pathways for improved charge transport [35]. Both attributes are linked to higher efficiencies. Post annealing provides an effective way to improve efficiencies after deposition is complete. Recent research has explored two types of post-annealing processes, thermal and solvent annealing [38].

Thermal annealing is the simplest way to change the morphology by utilizing heat to increase the mobility of the polymer chains. P3HT polymer chains rearrange to form inter-chain interactions, allowing an increase in stacking of the π-π orbitals [2,3,34]. This

increase in stacking leads to an increase in crystal ordering and improves hole mobility of P3HT. Also, thermal annealing drives a phase segregation between the two components[39]. This phase segregation is essential to improving the performance.

However, thermal annealing has limitations. Semi-crystalline conjugated polymers used in OPVs tend to have large glass transition temperatures, T_g. To overcome the high T_g of the polymer, a high temperature must be used to thermally anneal samples. Thermally annealing at too high of a temperature or for too long can cause polymer degradation or domain segregation. Annealing too long can lead to extensive domain segregation causing resistance to charge transport at the edges of the crystals [38]. This causes a decrease in the current flowing through the device, thus decreasing the performance.

A second type of post deposition annealing is solvent annealing. The major advantage of using solvent annealing is its ability to modify the nanoscale structure of the device in ways that other annealing techniques, such as thermal annealing, cannot accomplish. With solvent annealing, solvent slowly penetrates throughout the active layer altering the morphology[40]. By introducing solvent into the system, the mobility of both P3HT and PCBM is increased. The increased mobility allows P3HT to form long fibrillar structures, while PCBM aggregates form more slowly [34]. Wang et al. and Li et al. explored solvent annealing P3HT:PCBM samples using, 1,2-dichlorobenzene (ODCB). This study showed that solvent annealing can lead to improved ordering of P3HT and an increase in hole mobility [41]. Although research has been done using solvent annealing, the underlying mechanism is not well understood.

Unlike thermal annealing, where heat is the main contributor to morphology changes, solvent annealing has numerous factors to consider. One of these factors is solvent choice. Cho et al. focused on how quality of solvent affects morphology. Their findings showed that solvent annealing in poor solvents led to improved device performances [42]. Furthermore, Lu et al. researched the affect of varying the evaporation rates of carbon disulfide, CS_2, vapor on the morphology of poly(3-butylthiophene) (P3BT)/PCBM fi1lms. Their results showed that a slower evaporation rate allowed sufficient times for the morphology to evolve, improving the device performance [16].

Another factor to consider is the selective solubility of the BHJ components in the solvent vapor. By selecting a solvent only soluble to one component, one could selectively alter the morphology without affecting the entire active layer. Tang et al. first utilized this by a multistep solvent annealing process. By first exposing their samples to tetrahydrofuran (THF) vapor followed by CS_2 vapor, they were able to alter the aggregation of the PCBM in each solvent and increase the crystallinity of P3HT at the same time[13].

Thus, solvent annealing has unique features, which makes it optimal for use in the processing of OPVs. However, by introducing another component to the thin film system, changes in the morphology are strongly affected by both the polymer and the solvent used. Therefore, there is a need to understand how these factors affect the morphology of the bulk heterojunction. A better understanding of solvent annealing allows us to rationally improve the solvent annealing process.

1.8 Goals and Overview

In our experiments, the main goal is to understand and characterize the morphology of a P3HT/PCBM bilayer system. As previously reported, increasing the interfacial area between the two layers is an important aspect in improving the efficiency of the active layer. Solvent annealing allows solvent molecules to slowly penetrate into the bulk of the film, increasing the interfacial area. However, the solvent annealing process is not well-understood. We will study how solvent annealing affects the morphology of bilayers. To achieve this goal, we will look at three distinct systems:

I. A completely miscible PCBM:P3HT bilayer system.

II. A bilayer system slightly below the miscibility limit of PCBM in P3HT.

III. A bilayer system above the miscibility limit of PCBM in P3HT.

Increasing the loading of PCBM in the system alters the morphology and phase segregation, allowing us to track the importance of these parameters of the structural evolution and structure of the system.

In Chapter II, we use Grazing Incidence X-ray Diffraction (GIXRD) to determine the P3HT crystallinity and crystal size. We further explore the correlation between Raman "aggregation" and crystallinity. Chapter III focuses on using Near Edge X-Ray Absorption of Fine Structures (NEXAFS) to explore the composition at-or-near the surface of the PCBM/P3HT thin films. Finally, Chapter IV expands from the previous chapters and focuses on determining physical properties of thin polymer films. Expanding on the work done by Huang et al., we use an inexpensive setup to determine

the Young's modulus of polystyrene. By slightly altering the same methodology used to determine Young's modulus, we further attempt to establish a method to easily determine diffusion coefficients of gases through thin polymer films.

CHAPTER II
CORRELATING AGGREGATION AS DETERMINED BY RAMAN SPECTROSCOPY AND CRYSTALLINITY

2.1 Raman Spectroscopy

Raman spectroscopy is a widely used technique to explore vibrational modes of molecules. There are many unique advantages of this technique to characterize polymer photovoltaics. Raman is very sensitive to changes in the local ordering of the polymer. Small differences in conjugation length or miscibility of the system can be identified. Linking these subtle differences to deposition parameters and/or post annealing processes will improve our understanding of how they affect morphology. Different wavelengths of excitation are capable to selectively probe the polymer ordering in P3HT/PCBM devices[43]without interference from the PCBM.

Raman is also a non-destructive technique, allowing the in situ characterization of the change in morphology throughout the annealing process [44-47]. Exploring the annealing process with the selectivity of Raman provides useful insight into polymer ordering and domain segregation. Since conjugation length depends on the ordering and stacking of the π-π orbitals of the carbon-carbon double bond, the symmetric C=C stretching mode at 1445 cm^{-1} is of greatest relevance to device performance. This feature has been investigated with both non-resonance and resonance Raman Spectroscopy. Most studies use non-resonance conditions to avoid directly exciting the optimal electronic wavelength, which causes a strong fluorescent background and decreases the Raman

signal-to-noise ratio. However, on-resonant spectroscopy provides a method for more in-depth profiling of the active layer.

Tsoi et al. investigated the effect of resonant conditions on non-annealed and annealed regioregular P3HT/PCBM blends. The spectra of P3HT/PCBM excited at 633 and 488 nm are shown in Figure 2.1.1. By using an excitation wavelength of 633 nm, which is less than the optical band gap energy of the polymer, non-resonant conditions are reached [48]. As-cast samples and annealed samples show very little change in the peak position of the symmetric C=C stretching mode (1450 cm^{-1}). However at an excitation of 488 nm, a shift in peak position and a reduction of full-width at half maximum (FWHM) is noticed. This shift in peak position is hypothesized to be due to a change in ordering of the P3HT backbone.

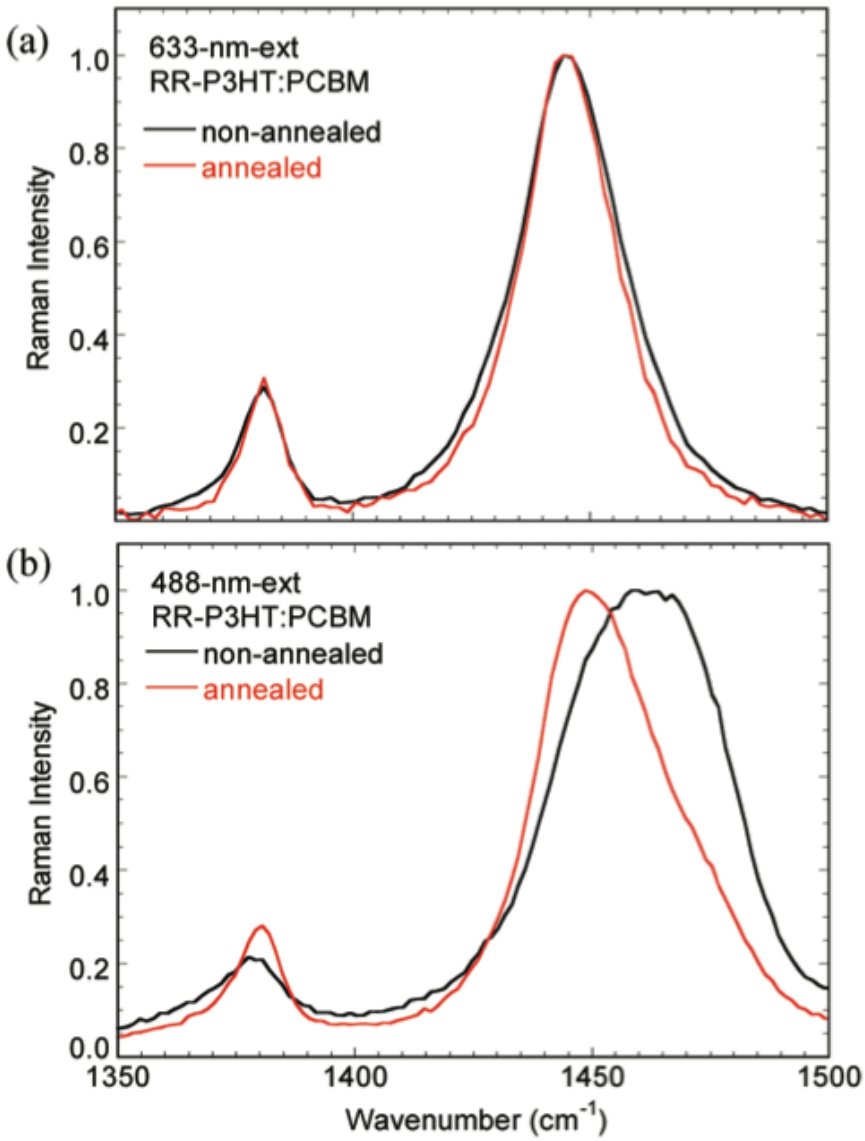

Figure 2.1.1: Raman spectra (C-C and C=C peaks) non-annealed and annealed regioregular P3HT:PCBM blends using a (a) 633 nm (b) 488 nm excitation wavelength [48]. A shift in peak position and FWHM is noticed at 488 nm, but not at 688 nm.

Grey et al. further explored the resonant Raman spectra of thermally annealed PCBM/P3HT blends. When attempting to fit the symmetric C=C stretching peak to an ideal Lorentzian, a shoulder appears in the peak for annealed samples [49]. The Raman spectra for the annealed and non-annealed samples are shown in Figure 2.2.2. This work

demonstrates that the peak at 1450 cm^{-1} is actually composed of two different components. The lower frequency component at 1445 cm^{-1} represents an "aggregated" P3HT C=C species (I_{agg}). This "aggregated" species has a lower transition energy due to increased inter- and intra-chain ordering of the P3HT [49]. The higher frequency component at 1470 cm^{-1} indicates an 'unaggregated' P3HT C=C species (I_{unagg}). "Unaggregated" refers to less π-π interactions and a shorter conjugation length.

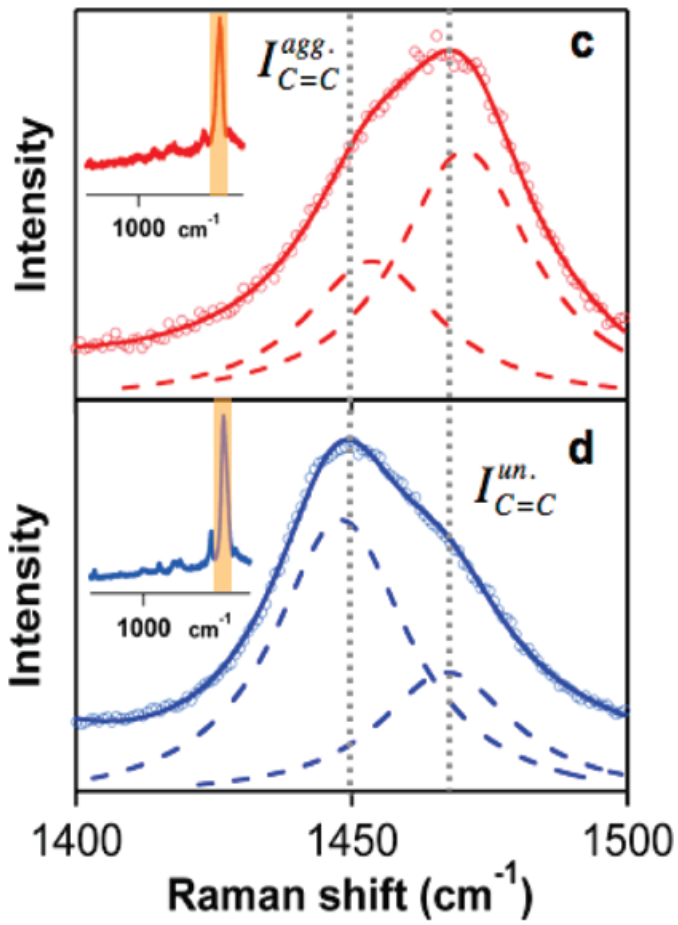

Figure 2.1.2 : Raman spectra of the P3HT C=C symmetric mode at 1450 cm^{-1}. The peak actually consists of two distinct peaks, an aggregated species at 1445 cm^{-1} and a unaggregated species at 1470 cm^{-1} [49].

It is not clear that addressing these two components as 'aggregated' and 'unaggregated' is an accurate representation of the structure of the system. The 'aggregated' species is a more ordered portion of the P3HT with a longer conjugation length and a more planar conformation. Likewise, the 'unaggregated' species is disordered, with shorter conjugation lengths and a more twisted conformation. The work of Grey et. al can be employed as a basis to use Raman spectroscopy to determine the degree of aggregation in P3HT in the solvent annealed PCBM:P3HT bilayer samples. By varying the concentration of PCBM in each sample, the effect of the presence of PCBM on the ordering of the P3HT chains can also be investigated.

To quantify the amount of 'aggregated' and 'unaggregated' P3HT in a sample, Grey et al. utilized the ratio of the intensities of each peak, R, as shown in Equation 2.1.1.

$$R = I_{agg}/I_{unagg} \quad (2.1.1)$$

This ratio is based on the assumption that the Raman scattering cross sections of both components are equal. We modified this relationship to more accurately monitor the percent aggregation in each species, which is shown in Equation 2.1.2.

$$PercentAggregation = \frac{A_{Agg}}{A_{Agg}+A_{Unagg}} \times 100 \quad (2.1.2)$$

In this equation, A_{agg} is the area of the Raman peak associated with the 'aggregated' species and A_{unagg} is the area of the Raman peak associated with the 'unaggregated' species. This equation only provides a quantitative measure of the percent aggregation if the Raman scattering cross-sections of both components are equal. However, even if this assumption is incorrect, this parameter still provides a qualitative measure of the amount of P3HT 'aggregation' in the system.

2.2 Grazing Incidence X-ray Diffraction (GIXRD)

X-ray based probes have been extensively used to provide useful information on the morphology of OPVs. Grazing Incidence X-ray Diffraction (GIXRD) is a well-established technique used to determine the crystallinity of polymers, including in OPVs. By using x-rays at the incidence angles below the critical angle, the crystalline properties and spacing of the crystals can be explored in a thin film sample [50]. Previous research has used GIXRD to establish a relationship between thermal [51,52] or solvent [53] annealing and an increase in coherent length of the crystalline P3HT domain. The average size of the P3HT crystals can be determined from the GIXRD pattern using Scherrer's equation:

$$CrystalSize = \frac{0.9\lambda}{\beta \cos(\theta)} \qquad (2.2.1)$$

where λ is the x-ray wavelength (1.54 Å), β is the full width at half maximum of the crystalline peak, and θ is the position of the crystalline P3HT peak.

P3HT crystalline domains can order themselves at a solid surface in one of two orientations, edge-on or plane on. A visual representation of each orientation is shown in Figure 2.2.1. In an edge-on orientation, the π-π stacking of P3HT chains occurs perpendicular to the substrate, while P3HT chains align parallel to the substrate in the face-on direction. A GIXRD spectrum of P3HT is shown in Figure 2.2.2. The peak at 2θ= 5.45° represents the (100) edge-on orientation, while a (200) peak at 2θ=10.66° indicates the face-on orientation. There is still some debate on which orientation is more desirable for improved photovoltaic performance. Although edge-on is preferred for transistor applications, the face-on orientation is desirable for new devices where charge

transport occurs normal to the electrode [54-56]. Regardless of the orientation, increasing crystallization and crystal size has been directly linked to improvement of OPV devices.

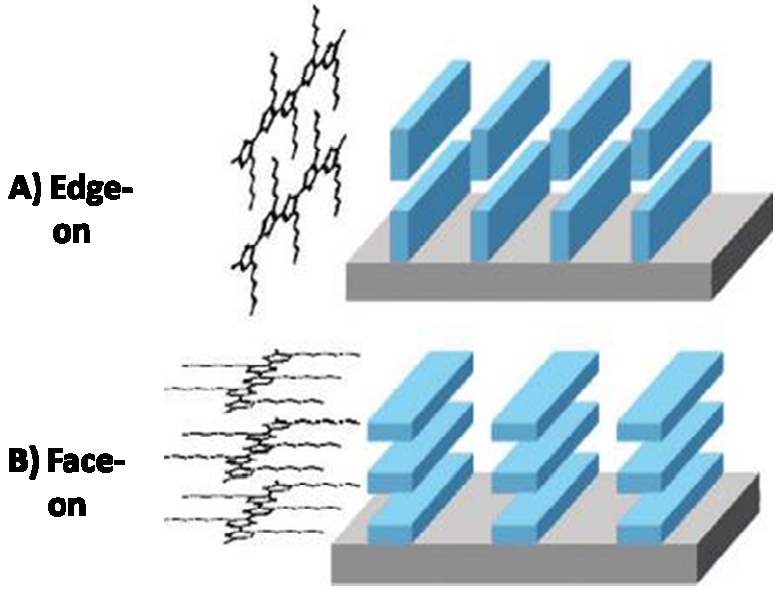

Figure 2.2.1: Illustration of orientation of A) Edge-on B) Face-on P3HT chains.

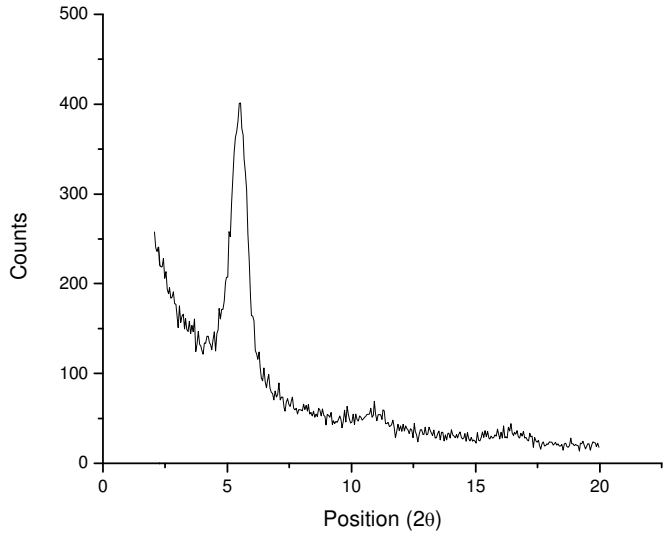

Figure 2.2.2: GIXRD spectra of P3HT

In the literature, researchers have proposed a direct correlation between the aggregation species as determined by Raman and the highly-ordered conjugated P3HT in crystalline domains. We will directly correlate the "aggregated" and "unaggregrated" species monitored by Raman spectroscopy to P3HT crystallinity as determined by GIXRD. Our goal is to look at this relationship two ways. First from a spectroscopic perspective, what structure does the "aggregated" species observed by Raman spectroscopy correlate to? Second from a polymer structure perspective, does the 'aggregated' species correlate to changes in the P3HT crystallinity or crystal size? If not, what structural component correlates to the optical shift in the Raman spectra?

2.3 Experimental Methods

2.3.1 Sample Preparation

Silicon wafers measuring 10 cm in diameter and 350-600 nm in thickness were purchased from Wafer World Inc. Square substrates measuring 2 cm by 2 cm were cut from the wafers and ultrasonicated (Cole-Parmer 8891) for 15 minutes in distilled water, acetone, and isopropanol. The substrates were then dried by a steady stream of nitrogen followed by 20 minutes in a UV/Ozone environment (Jelight Company Inc. Model No. 144 AX). This technique provides a clean, uniform layer of silicon oxide on the surface of the wafers.

Highly regioregularpoly(3-hexlthiophene) (P3HT) purchased from Rieke Metals (Regioregularity ≥ 95 %; M_w=20,000-30,000; PDI=2 provided by manufacturer) was dissolved in ortho-dichlorobenzene (ODCB) at concentrations of 10 mg/mL, 15 mg/mL,

and 27.5 mg/mL. Each solution was heated at 55° C overnight to assure all P3HT was dissolved in the solution. [6,6]-Phenyl-C61-butyric acid methyl ester (PCBM) purchased from Nano-C was dissolved in dichloromethane (DCM) at concentrations of 5 mg/mL and 10 mg/mL. The solutions were heated at 40 °C prior to spin coating. Both solutions were filtered through a 0.45 µm PTFE syringe filter to eliminate any non-dissolved particles.

2.3.2 Spin Coating

Spin coating is a simple technique to create uniform thin films, often used in research laboratories. Figure 2.3.1 shows a schematic illustration of the spin coating process. By using centripetal force, a thin layer of polymer with uniform thickness is coated on the surface of a substrate. There are three main parameters to consider when spin casting samples. Spin speed and the concentrations of the solution are key parameters used to adjust the thickness of the final film. Since excitons can only travel 10-20 nm [3,17], it is important to be able to create a thin uniform active layer. A thin film is easily obtained using spin coating. The last parameter is spin time, where spin time affects how quickly the film dries. By allowing the sample to spin longer, more solvent evaporates leading to less time for the system to phase separate.

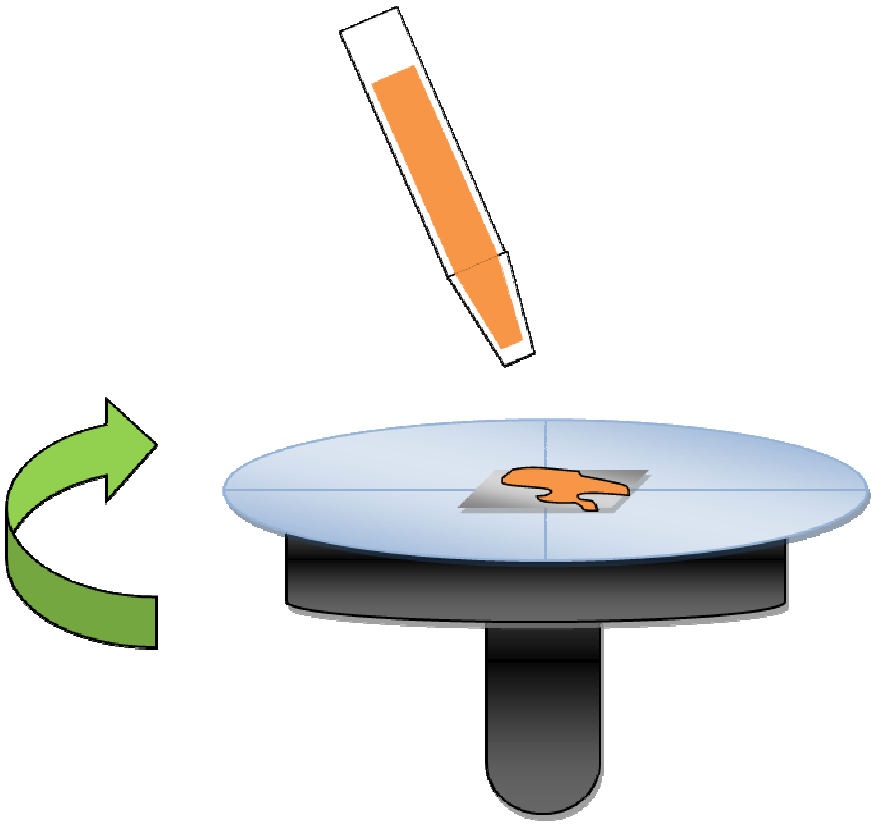

Figure 2.3.1: Illustration of spin coating process.

P3HT was first deposited on top of the Si substrate by spin-coating P3HT solutions at 1200 rpm for 90 seconds. The sample was then allowed to further dry in a nitrogen-rich environment for 20 minutes to ensure all ODCB had evaporated. PCBM was then spun from a solution in dichloromethane on top of the P3HT layer at 4000 rpm for 10 seconds to create a bilayer architecture. This 'bilayer' sample was placed under vacuum (30 mmHg) for 20 minutes to allow sufficient time for the DCM to evaporate. A list of the processing parameters and resulting thicknesses of the10/90, 20/80, and 40/60 PCBM:P3HT bilayer samples are shown in Table 2.3.1

Table 2.3.1: Spin coating processing parameters and film thicknesses of 10/90, 20/80, 40/60 PCBM:P3HT bilayer samples.

Sample (PCBM/P3HT)	P3HT (mg/mL)	Spin Speed & Time	Thickness (nm)	PCBM (mg/mL)	Thickness (nm)	Spin Speed & Time
40/60 Bilayer	10	1200 rpm for 90 seconds	50	10	34	4000 rpm for 10 second
20/80 Bilayer	15		80	5	22	
10/90 Bilayer	27.5		155	5	22	

2.3.3 Solvent Annealing

As previously mentioned, increasing the P3HT:PCBM interfacial area in bilayer devices is essential to improve the photovoltaic efficiency. Solvent annealing allows the solvent to slowly penetrate through the layers, allowing the layers to mix, and presumably creating pathways for charge transport. An illustration of the apparatus that was used in the solvent annealing process is shown in Figure 2.3.2. ODCB was placed in the bottom of a 100 cm vertical column. After equilibration, this creates a constant solvent vapor pressure gradient, where 0 cm from the top represented 0% solvent vapor pressure (SVP) and 100 cm down the column equals 100% SVP. The column was allowed to equilibrate for four hours prior to using it in the solvent annealing. The samples were set at a height of 90 percent SVP and annealed for a predetermined time. After solvent annealing, samples were placed in a vacuum oven overnight to allow the solvent to completely evaporate.

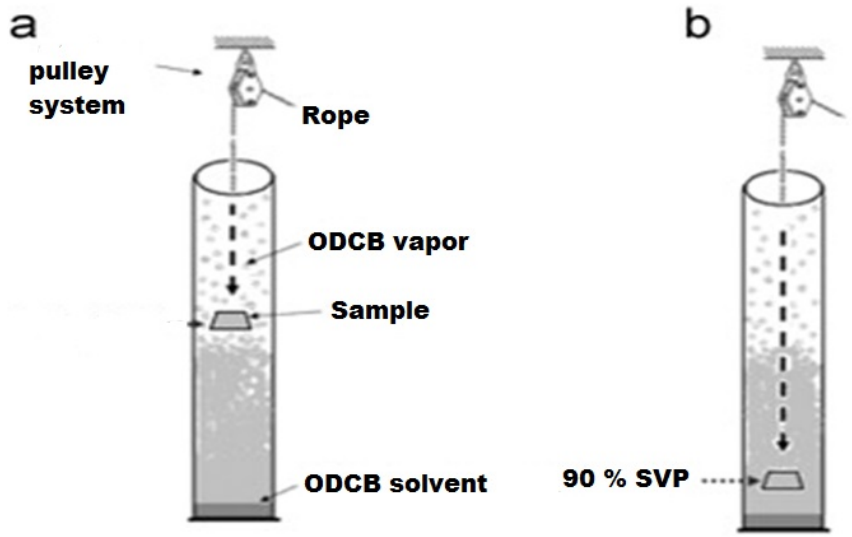

Figure 2.3.2: Schematic diagram of solvent annealing apparatus where a) sample is lowered into the column filled with ODCB vapor b) sample is set 90 cm down the column equivalent to 90% SVP [57].

2.3.4 Raman Spectrometry

A homemade Raman set-up, shown in Figure 2.3.3, was used. A Ti:sapphire laser (Spectra-Physics, Tsunami) that is pumped with a 532 nm Nd:YAG laser (Spectra-Physics, Millenium XV) capable of tunable operation in the NIR spectrum was used for excitation. The laser was tuned to a wavelength of 942 nm, as measured by a NIR/UV-Vis spectrometer (Ocean Optics, USB4000). The laser beam was sent through a frequency doubler (Spectra-Physics) producing the desired wavelength of 471.5 nm. In the inverted microscope (Nikon, Ti-U), an 80/20 beam splitter (Semrock) reflects the excitation beam through an objective (Nikon, 20x, NA=0.5), which is focused on the sample. The output of the laser measured at the sample interface on the microscope stage

was 0.1 mW. The objective collects the back-scattered light, transmitting it through the beam splitter, and then to either the eyepiece or a spectrometer (Acton, Princeton Instruments) with a back-lit CCD LN-cooled detector (Princeton Instruments , PIXIS 100). Samples were rastered to eliminate changing the morphology by the laser intensity. By rastering the sample, an average of the optical response of the sample is obtained. A Raman spectrum of liquid cyclohexane was used to calibrate the spectrometer. The Raman shift was calculated using a homemade program.

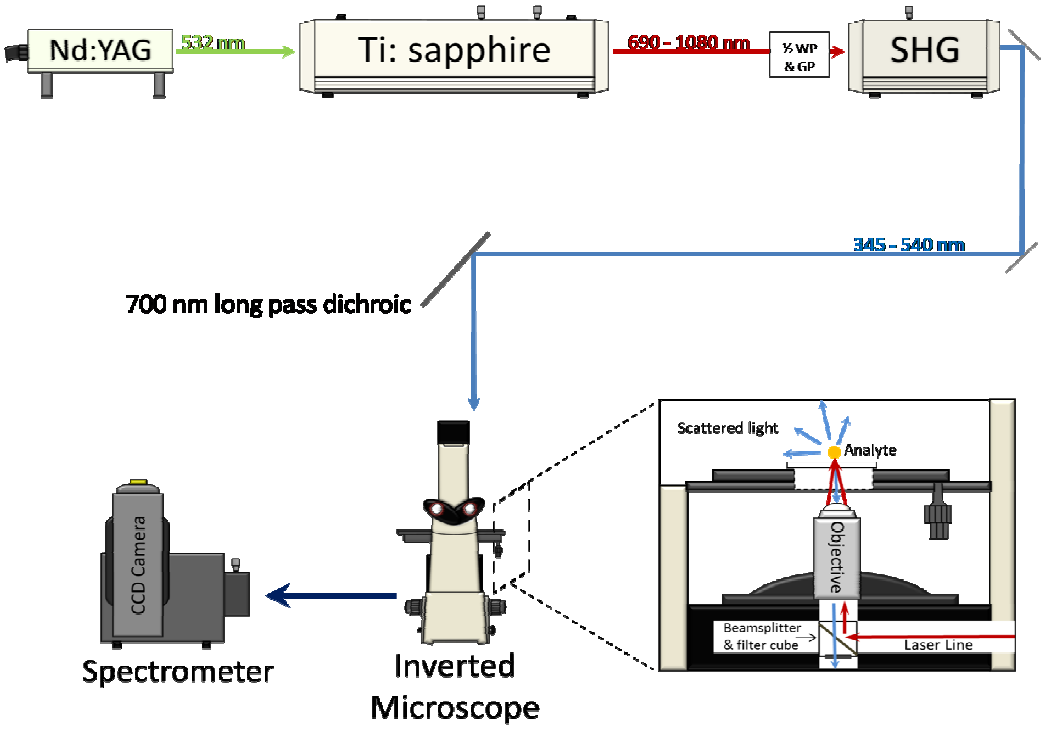

Figure 2.3.3: Diagram of the Raman Setup [58].

2.3.5 GIXRD

X-ray diffraction patterns of randomly oriented thin films were collected by a Phillips X'pert Pro diffractometer using grazing incidence geometry. Power levels were set to 45 kV tube voltage and 40mA tube current. The angle of incidence was set to 0.3° for all samples. Positions from 2 to 20° (2Θ) were scanned using a continuous scan mode with a step size of 0.05° and a time per step of 0.5s. Each spectrum was normalized to account for the differences in concentration of P3HT in each sample. The P3HT diffraction peaks were analyzed by X'PertHighScore™ software.

2.4 Results and Discussion

2.4.1 Correlating Raman "Aggregation" and Crystallinity

For our experiments, three distinct bilayer systems were used to study the relationship between crystallinity and the aggregation of the polymer as determined by Raman spectroscopy. As previously discussed, solvent annealing allows us to selectively alter the morphology of the system. The penetration of the solvent into the thin film allows the P3HT and PCBM to equilibrate, where the final morphology and polymer ordering in a miscible P3HT:PCBM system will differ from that in a phase separated P3HT:PCBM system.. Thus, we can track changes in polymer ordering and crystallinity in samples that vary in their extent of phase separation.

The first system that was studied was a 10/90 PCBM:P3HT bilayer sample. This sample is below the loading limit of PCBM in P3HT. The second sample was a 20/80

PCBM:P3HT bilayer. At this concentration, the system is approaching the miscibility limit of 22 % PCBM in P3HT [33]. Finally, a 40/60 PCBM:P3HT sample, which is phase segregated, was examined. Each sample was solvent annealed for 30,60 and 90 minutes in ODCB at 90 percent SVP. The GIXRD spectra for all samples are shown in Figure 2.4.1 (shown in Appendix). The areas of the d100 crystalline peak in the GIXRD spectra for the three different samples are plotted in Figure 2.4.2 as a function of solvent annealing time. Also, the data for the pure P3HT samples cast from the corresponding concentrations to form films with commensurate thicknesses of 27.5 mg/mL (155 nm), 15 mg/mL (80 nm), and 10 mg/mL (50 nm) are shown in the same Figure 2.4.2.

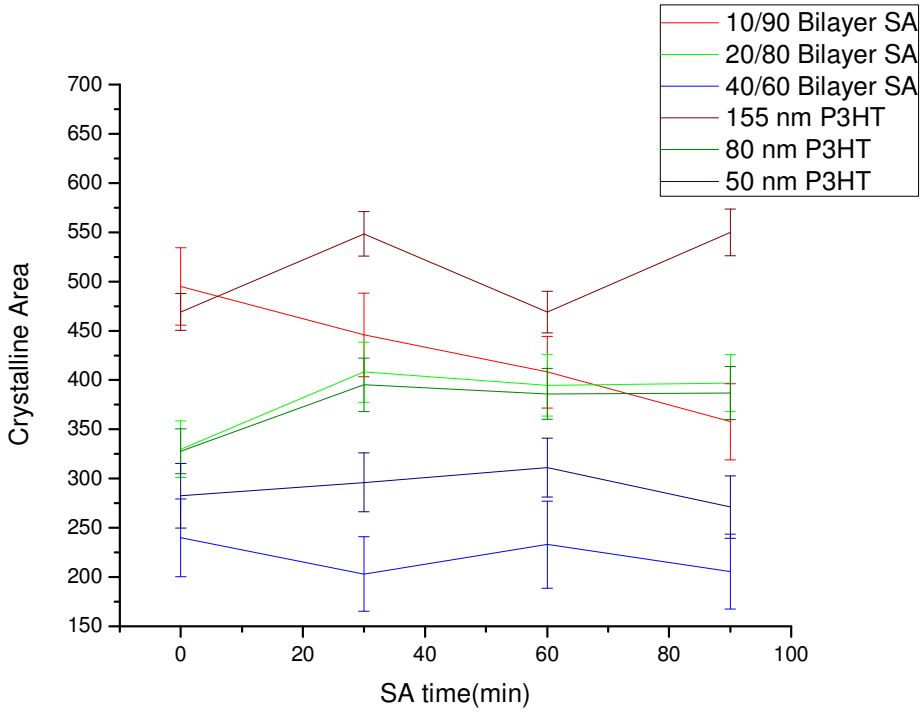

Figure 2.4.2:Area of the P3HT crystalline peak of 10/90, 20/80, and 40/60 PCBM/P3HT bilayers solvent annealed for 30,60, and 90 minutes in ODCB at a SVP of 90%.

We first introduce a small amount of PCBM into the P3HT in the 10/90 bilayer sample. At this concentration, all of the PCBM should be miscible in the system. As solvent annealing time increases, the 10/90 bilayer shows a decrease in the P3HT crystallinity. Comparing these results to those of the 155 nm pure P3HT, we see two distinctly different trends. Unlike the 155 nm pure P3HT film where solvent annealing allows P3HT chains to form more crystalline domains, introducing PCBM molecules into the system inhibits the crystallization of P3HT causing the shown decrease in crystallinity. It appears the PCBM acts as a solvent molecule, dissolving smaller crystals of P3HT. These results indicate that introducing solvent into the system swells the P3HT, allowing PCBM molecules to penetrate throughout the film dissolving the smaller crystals.

The next system explored is near the miscibility limit of PCBM in P3HT. Comparing the 20/80 bilayer sample to the 80 nm thick pure P3HT film shows the crystallinity of the P3HT in the 20/80 bilayer is very similar to the pure P3HT film, and thus is not influenced by introducing the PCBM into the active layer. As we solvent annealing both samples, smaller P3HT crystals are being dissolved by the ODCB solvent molecules while larger crystals are forming. This would account for the increase in the crystallinity we see in the samples.

Finally, we explored a 40/60 bilayer system, which is above the miscibility limit of PCBM in P3HT. As we solvent anneal the 40/60 bilayer sample, there is little to no change in the amount of P3HT crystallinity. At this loading of PCBM, the system is now composed of P3HT rich domains, an amorphous region containing both PCBM and P3HT, and also PCBM rich domains. This phase segregation system limits the

crystallization of larger P3HT domains. Also, solvent molecules may dissolve the larger P3HT crystals as smaller P3HT with more freedom continue to grow. This would explain no change in the crystalline area.

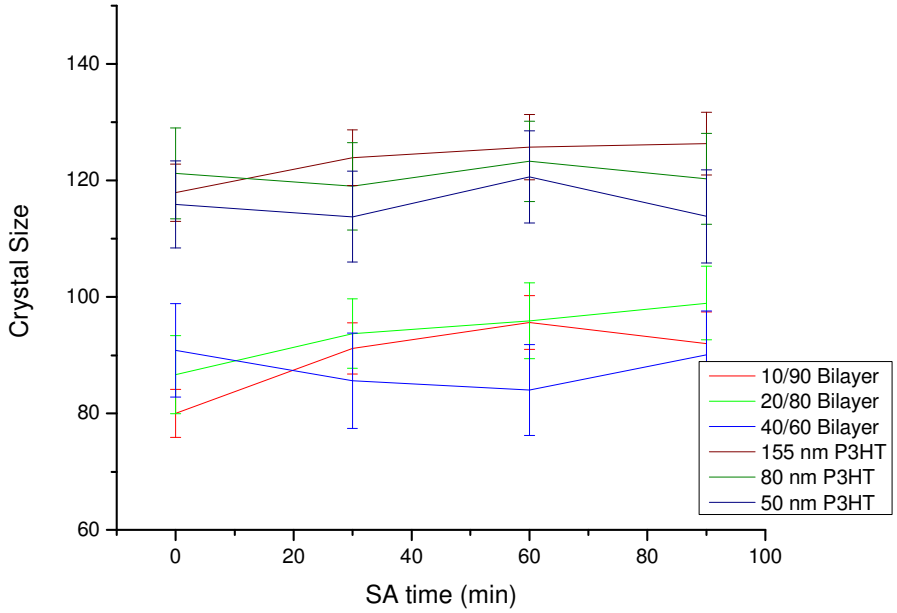

Figure 2.4.3: Average crystal size of 10/90, 20/80, 40/60 PCBM/P3HT bilayer samples solvent annealed in ODCB for 0, 30, 60, and 90 minutes. Crystal size was calculated using Sherrer's equation.

To further understand how solvent annealing affects the ordering of the P3HT in the film, we need to take a closer look at the crystal size. By using Sherrer's equation (Equation 2.2.1), the average crystal size of the 10/90, 20/80, and 40/60 bilayers are determined and plotted in Figure 2.4.3 as a function of solvent annealing time. As previously mentioned, a decrease in the crystallinity of 10/90 bilayer samples indicated

that PCBM inhibits P3HT crystallization. However, an increase in the crystal size is noticed as solvent annealing time increases in this sample. By introducing PCBM into the system, an amorphous region containing both PCBM and P3HTexists. This region may dissolve numerous smaller adjacent P3HT crystalline domains, while larger crystalline domains are unaffected. This process would explain the decline in crystallinity of the system but an overall increase in the crystal size.

Looking at the crystal size of the 20/80 bilayer in Figure 2.4.3, we see an increase in the crystal size as the solvent time increases. However, the crystallinity for the 20/80 sample remained constant after 30 minutes of annealing. As in the 10/90sample, these results can be explained by smaller P3HT crystals being dissolved by ODCB and/or PCBM molecules, while larger P3HT crystal continue to grow. This would account for larger crystals size and also the plateau observed in the crystallinity.

Finally, the 40/60 bilayer sample shows no change in the crystal size as we anneal the sample. Since the system is above the loading limit of PCBM in P3HT, the 40/60 bilayer forms a phase segregated system. As we solvent anneal the film, P3HT rich regions form and surrounded by PCBM rich domains and/or amorphous regions contain both components. Due to the multiple phases in the system, there is minimal space for larger crystals to continue to grow. Solvent molecules are dissolving larger crystals while the P3HT chains in smaller domains have more confirmation freedom and continue to grow. This would account for no change in the crystal size.

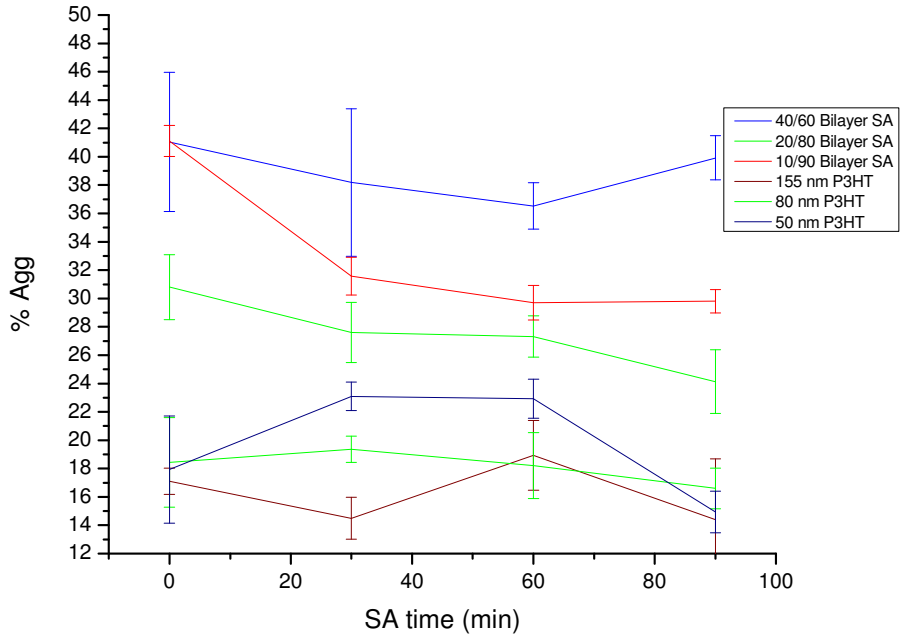

Figure 2.4.4: Percent aggregation of P3HT in 10/90,20/80, 40/60 PCBM/P3HT bilayer samples solvent annealed for 0, 30, 60, and 90 minutes in ODCB at a SVP of 90%.

To begin to determine the relationship between Raman "aggregation" and P3HT crystallinity, we need to directly compare the two results. The percent aggregation as determined from Raman spectroscopy for each sample was determined using Equation 2.1.2. The percent aggregation in the 10/90, 20/80, and 40/60 PCBM:P3HT solvent annealed bilayers are shown in Figure 2.4.4 as a function of solvent annealing time. Comparison of the 'aggregation' and crystallinity shows that there are multiple differences between the two. The first is observed in the behavior of the 50 nm pure P3HT sample. Figure 2.4.4 shows an increase in the percent aggregation of the 50 nm pure P3HT sample after 30 minutes solvent annealing. The percent aggregation then remains constant until it decreases after solvent annealing for 90 minutes. However, the

crystallinity of the sample, as shown in Figure 2.4.2, remains constant through the annealing process. The 20/80 bilayer sample also shows a difference between the crystallinity and the percent aggregation. The crystallinity of the sample increases in the first 30 minutes before reaching a constant value. Conversely, the percent aggregation shows a decline in the amount of the aggregated species as we anneal the sample. Lastly, looking at the two systems below the miscibility limit(the 10/90 and 20/80 bilayer samples), a decrease in the aggregated species is observed with solvent annealing time. Increasing the loading of PCBM in the system has been known to cause more disorder in the packing of the P3HT chains, limiting the crystallinity [34]. If the "aggregated" species correlates directly to crystallinity, we would expect a decrease in the aggregation as we increase the loading of PCBM. Yet, the highest percent aggregation is shown in the 40/60 bilayer sample.

It becomes apparent that the crystallinity of P3HT and the "aggregated" species shown in Raman cannot be directly correlated. The question then arises if aggregated species do not directly represent crystallinity, what is the relationship? We believe to answer this question a closer look at the morphology of P3HT is needed.

As annealing time increases, the highly-ordered P3HT crystal domains differ greatly from the disordered amorphous region. Yet, both are somehow connected. The connecting region must have some ordering present. Could these slightly ordered, connecting polymer segments factor into the aggregated species as monitored by Raman Spectroscopy? Figure 2.4.5 shows a proposed morphology of the P3HT that includes these connecting polymer segments. In this model, there are not only amorphous regions with less ordered P3HT and crystalline regions of P3HT with chain segments with more

order, but also a third conformational structure with an intermediate ordering that links the two together. This conformational disordered segment is known as a “condis crystal”, where the structure permits liquid-like ordering while retaining orientational order [59]. The condis crystal, with an intermediate amount of order, will have a different structure and thus smaller conjugation length than the ordered polymer in the crystal but a larger conjugation length than the amorphous polymers. This intermediate range of molecular order may account for the "aggregated" species shown in Raman spectroscopy.

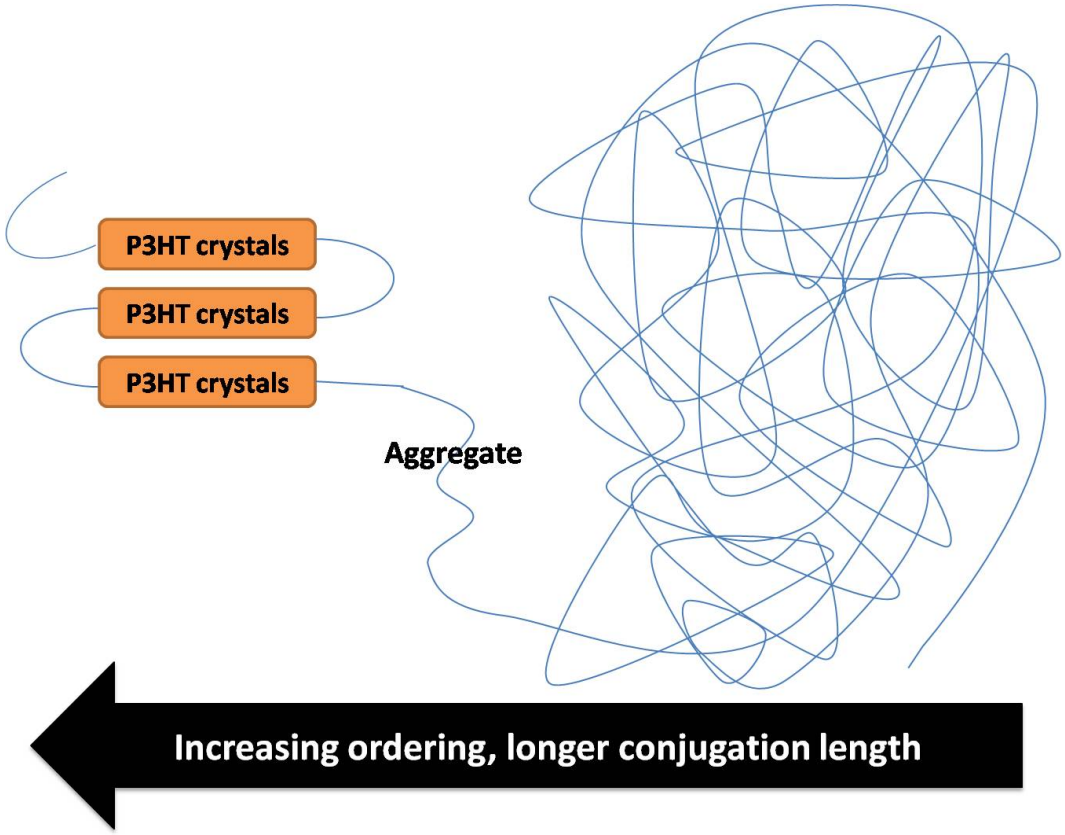

Figure 2.4.5: Illustration of three types of ordering of P3HT. The amorphous region of P3HT represents disordered, shorter conjugated chain segments. The P3HT crystals are highly ordered, longer conjugated chains. The intermediate with some ordering between the two regions represents the aggregated species shown in Raman.

To quantify the amount of this intermediate ordered structure that exists in a sample, we introduced a new term that is related to the surface area of the crystals that is present in a sample. This measure of crystal surface area is determined by the equation:

$$SurfaceArea = {}^{Crystallinity}/_{CrystalSize} = {}^{Volume}/_{Length} \quad (2.4.1)$$

This takes into account the volume of the crystal, as measured by the polymer crystallinity and a characteristic length scale of the crystal, the crystal size. Figure 2.4.6 shows the calculated surface area of the 10/90, 20/80, and 40/60 bilayer samples as a function of solvent annealing.

The 10/90 PCBM:P3HT bilayer shows very good correlation between the surface area of the crystal and the percent aggregation, where there is a decrease in the surface area, corresponding to an increase in crystal size. This suggests fewer larger crystals make up the P3HT domain. The decrease in the surface area of crystals correlates well to the "aggregated" species as determined by Raman, shown in Figure 2.4.4.

The 20/80 bilayer shows no change in surface area as annealing time increases, which correlates well with very little change observed in the percent aggregation with solvent annealing shown in Figure 2.4.4.

Finally, comparison of the Raman results and surface area of the 40/60 bilayer sample shows only small changes in the surface area with solvent annealing. The percent aggregation of the sample also shows no change with solvent annealing, which correlates with the flat curve shown in Figure 2.4.6, which shows the consistency of the amount of surface area in this sample with solvent annealing.

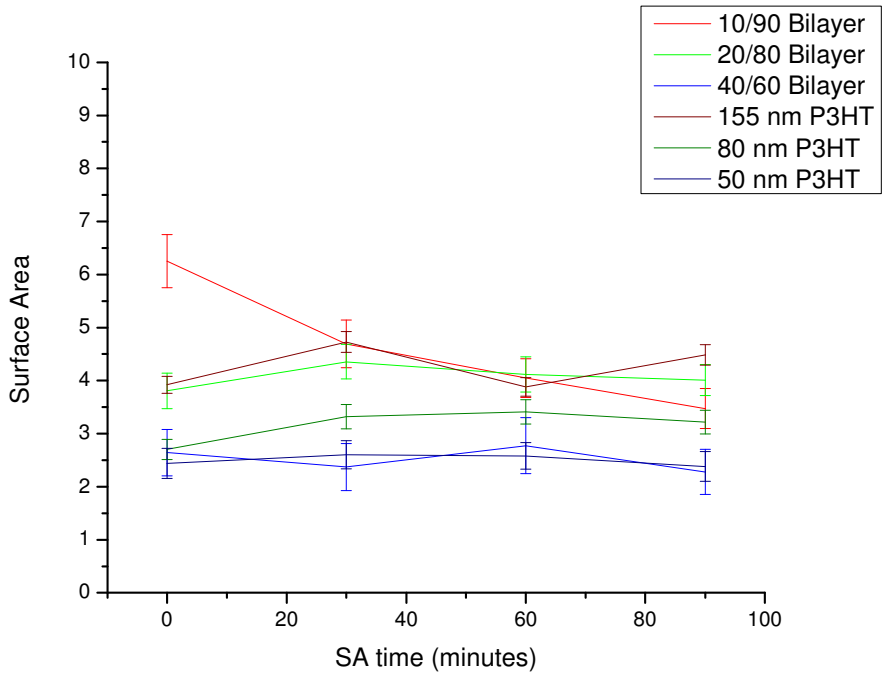

Figure 2.4.6: Surface area of 10/90, 20/80, and 40/60 PCBM/P3HT bilayer samples. Surface area refers to area between the crystalline and amorphous phases.

2.4.2 Impact of Wavelength Choice on Measured Percent Aggregation

As previously mention, on-resonance Raman is key to exciting the "unaggregated" peak [46]. We tested the importance of the choice of wavelength, and resonance, on the experimental determination of the amount of aggregation present in the solvent annealed 20/80 bilayer systems. The resulting percent aggregation of the sample as a function of solvent annealing time for excitation wavelengths of 472, 514, and 532 nm are shown in Figure 2.4.7. As expected, the on-resonance excitation wavelength of 472 nm shows a clear decrease in aggregation with solvent annealing time, as is also shown in Figure 2.4.4. However, when the excitation wavelengths are changed to 514 or

532 nm, the data become very scattered. This is primarily because the presence of a separate shoulder to the peak is minimal or absent. Therefore, we conclude that exciting P3HT at472 nm is required to accurately monitor the extent of aggregation in these samples. The result for the samples that were excited at514 and 532 nm is an artifact that comes from forcing what is essentially a single peak to fit to multiple peaks.

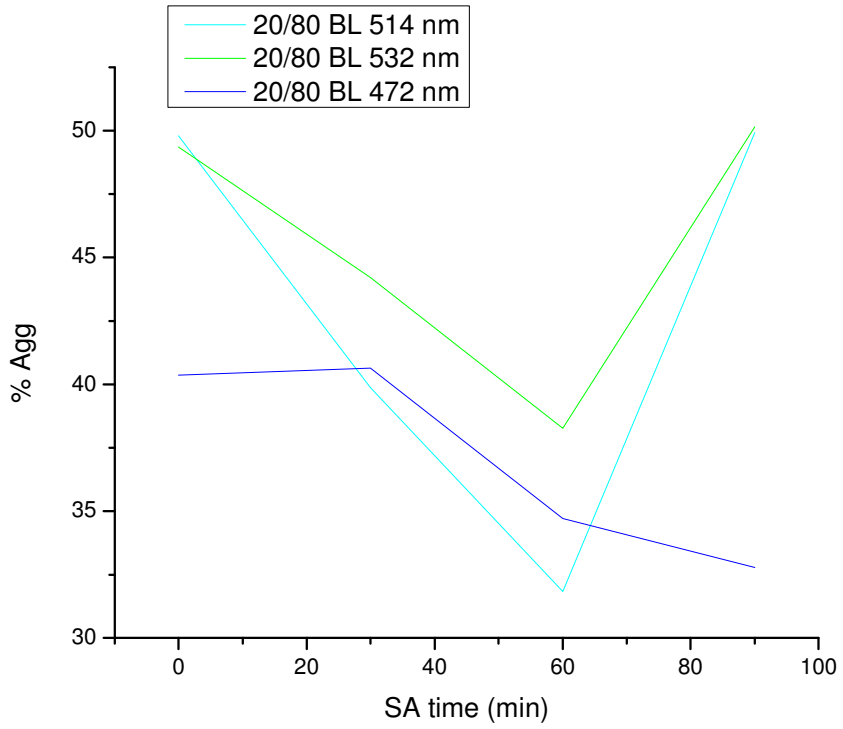

Figure 2.4.7: Percent aggregation of 20/80 PCBM:P3HT bilayer solvent annealed for 0,30,60, and 90 minutes in ODCB at 90 % SVP. The resulting percent aggregation was obtained by an excitation wavelength of 472, 514, and 532 nm.

CHAPTER III
NEAR EDGE X-RAY ABSORPTION OF FINE STRUCTURES

Previously mentioned techniques penetrate through the bulk, and therefore do not provide information on what is occurring to the morphology at certain depths throughout the active layer. High-resolution spatial mapping is needed to fill the gaps not provided by GIXRD or Raman spectroscopy. Recently, Near-edge X-ray Absorption of Fine Structure (NEXAFS) has become a popular tool to fill these gaps and characterize the structures of OPVs near surfaces [60, 61]. NEXAFS was first introduced in the 1980s as a method to examine the structure of molecules and how they orient themselves at an interface [60]. In NEXAFS, core shell electrons are excited by soft x-rays to unfilled molecular orbitals. The energy difference between the two levels generates a spectrum like the one shown in Figure 3.1.1. Unlike GIXRD, the angle of incidence of NEXAFS not only is capable of exploring the bulk, but is also a depth-dependent probe of the structure. For instance, at a bias of -50 V, the technique penetrates 10-12 nm into the film [36, 60]. As the bias increases to -125 V and -225 V, 3-9 nm and 1-2 nm from the surface are investigated [36, 60], respectively. This provides an advantage of probing throughout the top of the active layer to understand how the P3HT or PCBM is being altered near the surface as annealing is taking place.

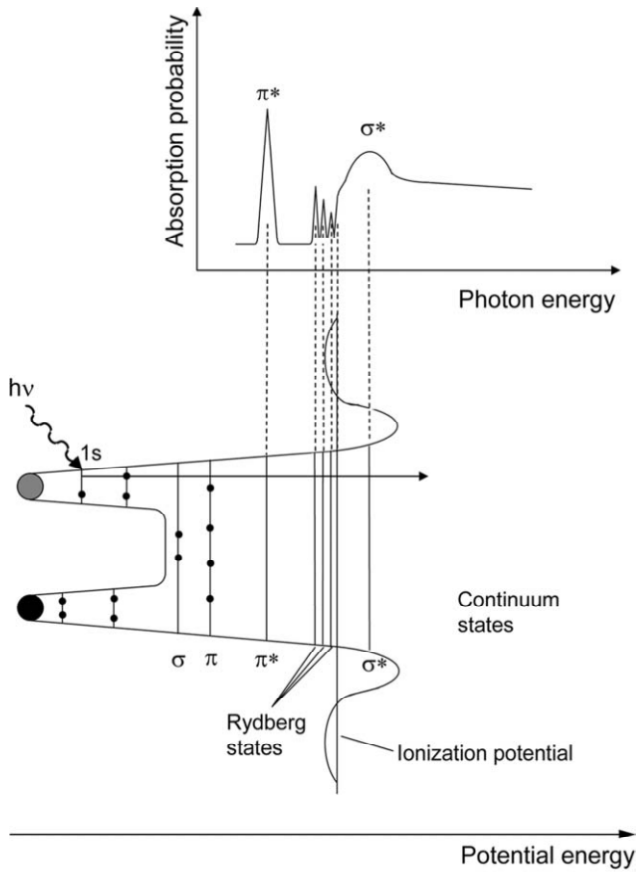

Figure 3.1.1: Illustration of how NEXAFS spectra are produced. Soft x-rays excite core shell electrons to unfilled anti-bonding molecular orbitals. The energy difference between the core level and excited energy levels produce a spectra. Key features of fullerene/thiophene OPVs are the π* and σ* transitions [60].

NEXAFS is very sensitive to chemical structure. Two unique features in the NEXAFS spectrum of thiophene/fullerene systems are the π* and σ* transitions. Since there is a large difference in energies between σ and σ* transitions, a broadening of the peak leads to a difficult data analysis and provides little useful information [60]. However, the π to π* transition creates a distinct, sharp peak providing useful insight into the structure of the samples. One of the unique features of PCBM:P3HT samples is the

slight difference in the positions of the π* peaks of P3HT and PCBM. The peaks at 285.0 and 286.46 eV are C=C π* resonances from the PCBM, while the peak at 285.85 eV is the C=C π* resonance from P3HT. By fitting two reference spectra (pure P3HT and pure PCBM) to a sample spectrum at a "magic" angle of 55°, the composition of the sample at the surface can be determined [36,60,62].This angle is called a "magic" angle because it is orientation independent and allows us to look at the sample without interference [62]. The composition of the sample at different depths spatially maps the movement of P3HTand PCBM with either thermal or solvent annealing, to document how these procedures alter the distribution of both components near the surface.

Neutron reflectivity (NR) is also a technique capable of probing the depth profile of P3HT/PCBM samples. By fitting of the neutron reflectivity profiles, a depth profile of the components normal to the surface can be determined. Also as long as there is a contrast between components, their segregation to the interfaces can be determined. This provides insight into the pathways available for charge separation and transport in the systems [63]. Since there is a distinct contrast between the scattering of the protonated conjugated polymer and the carbon-based PCBM molecules, NR is capable of mapping the movement of PCBM and allows us to study the structure, interfaces, and morphology of our systems. By correlating NEXAFS to NR data, we can better understand what changes near the air/surface interface occur upon annealing.

As we have previously discussed, solvent choice, deposition conditions, and post-deposition annealing can all affect the orientation of the P3HT in the thin film. Correlating P3HT crystal orientation at the electrode surface to deposition and annealing conditions will provide important information that will enable the rational improvement

of OPV devices. However, GIXRD with a 1-dimensional detector only provides information about the average crystal structure occurring in the film, but does not differentiate between crystals that are aligned edge-on or face-on. NEXAFS provides a direct measure of the orientation of P3HT crystals at the surface. Changing the incidence angle of the x-rays on the sample reflects the orientation of the sample in the spectrum. By plotting the π^* intensity as a function of $\sin^2\theta$ for at least 5 different incidence angles, the dichroic ratio, R, can be determined by the slope of the line [15]. An R value of 0 designates a completely disordered system, while a typical P3HT:PCBM that is well-ordered, with edge-on orientation will show R values of 0.25 to 0.30 [60]. Determining the orientation will allow us to better understand how the crystalline domains are forming and determine how the processing conditions are affecting our systems.

NEXAFS also provides the composition of the thin film at the surface. This information can be interpreted to indicate how deposition conditions, processing details, and annealing parameters alter the depth profile and morphology of the P3HT/PCBM system, and can be correlated to neutron reflectivity data.

3.1 Experimental Methods

NEXAFS measurements were taken on beamline U7A at the National Synchrotron Light Source (NSLS) at Brookhaven National Laboratory by Dr. Ron Quinlan. The schematic shown in Figure 3.1.2 shows the instrumental setup to obtain the data. The partial electron yield (PEY) signal was collected using a channeltron electron multiplier with an adjustable entrance grid bias (EGB). A negative bias of 50 V was

applied to prevent low-energy photoelectrons from reaching the detector. Angles of 20°,44°,55°,70°, and 80° with respect to the surface of the substrate were collected by rotating the sample holder with respect to the incident beam in the plane of incidence. The monochromator energy scale was calibrated using the C K-edge π* transition of graphite, located at 285.5 eV.

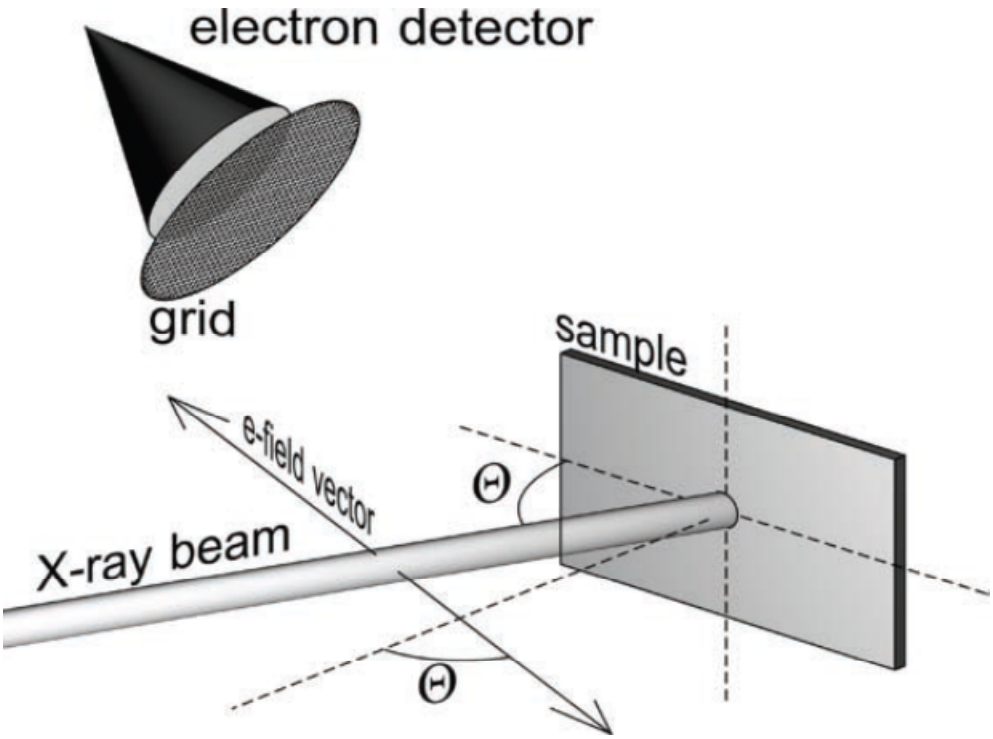

Figure 3.1.2: Schematic illustration of NEXAFS [36]. The sample is tilted at an incidence angle θ. Data was taken for five different incidence angles of 20°,44°,55°,70°, and 80°.

3.2 Results and Discussion

3.2.1 NEXAFS on Thermally annealed Bilayer samples

A NEXAFS spectrum for a 20/80 PCBM:P3HT as-cast bilayer sample is shown in Figure 3.2.1. Incidence angles of 20°, 44°, 55°, 70°, and 80° were collected for each sample. An illustration of the sample preparation and processing is shown in Figure 3.2.The P3HT layer was deposited on the Si substrate and thermally annealed at 150°C for 0, 20 and 60 minutes. A layer of PCBM is then cast onto these films, where the samples formed immediately after casting the PCBM layer, are denoted "as-cast".

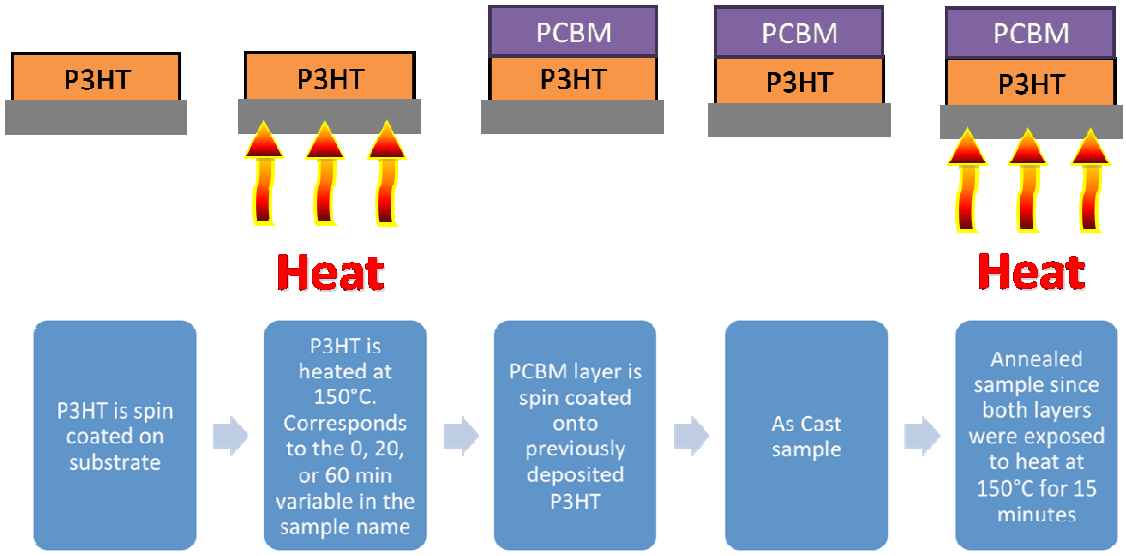

Figure 3.2: Illustration of sample preparation and annealing process.

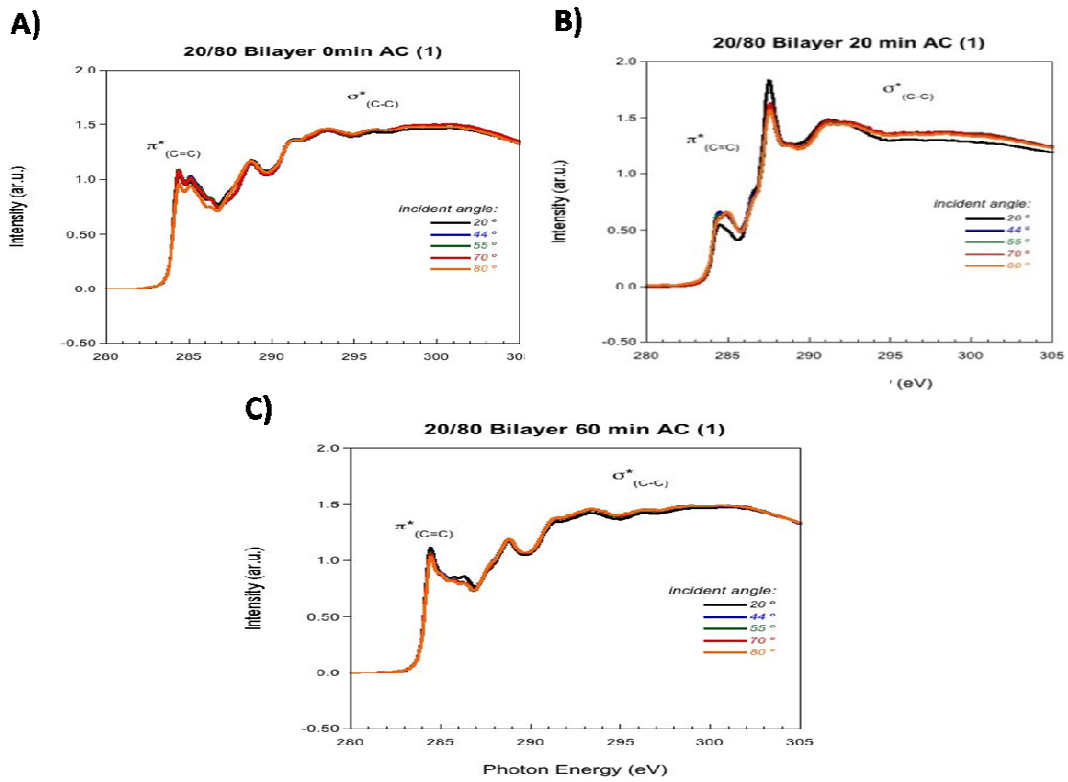

Figure 3.2.1: NEXAFS spectra for 20/80 PCBM:P3HT bilayer sample. P3HT layer was thermally annealed at 150°C for A) 0 B) 20 and C) 60 minutes. Each spectra was taken at incident angles of 20,44,55,70, and 80 degrees.

By fitting the samples to the spectra of the pure P3HT and pure PCBM at the orientation-independent "magic" angle of 55°, the percent P3HT at each depth was determined, from the data that is shown in Figure 3.2.2. The -50 V bias (top 1-12 nm), -150 V bias (top 1-9 nm), and -225 V(top 1-2 nm) were used to probe the composition at-or-near the surface of the film. Initially, spin casting the PCBM onto unannealed P3HT layer(0 minute 20/80 AC sample shown in Figure 3.2.2) creates a film with a majority of PCBM molecules distributed throughout the top 12 nm. NR conducted by our group verifies that PCBM penetrates throughout the film during the deposition process. Li et al. determined that the time at which the solvent evaporates during the spin-casting process

is between 20 to 80 seconds after casting [64]. Therefore in this drying time, the presence of the solvent allows the PCBM molecules to penetrate throughout the film.

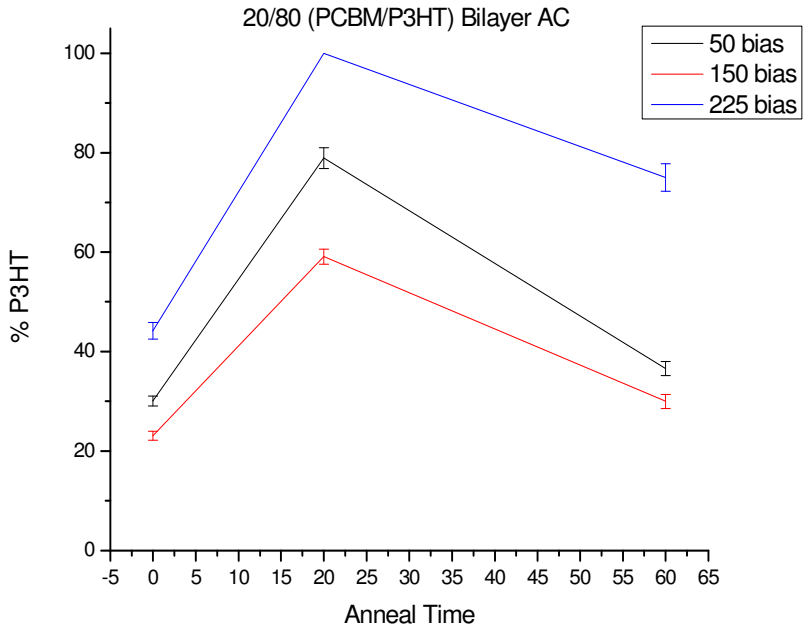

Figure 3.2.2: Percent of P3HT of 20/80 PCBM:P3HT bilayer. Three biases of 50 V bias (top10-12 nm), 150 V bias (top 3-9 nm), and 225 V(top 1-2 nm) were used.

Once the P3HT layer is annealed for 20 minutes before casting the PCBM layer, an increase in the P3HT chains at the air interface is observed. Neutron Reflectivity (NR) data also confirms that, after just the P3HT layer for short times prior to PCBM deposition, P3HT resides at the air/surface interface in the as-cast samples. We also see an increase in the percentage of P3HT in the -150 V and -50 V biases. Although heating the P3HT layer induces crystallization, there is still an amorphous region at the bulk

interface. This amorphous region allows PCBM to migrate away from the surface, causing the shown increase in the P3HT near the surface.

After the P3HT layer has annealed for 60 minutes prior to PCBM deposition, the data indicates that the surface is still composed of a majority of P3HT. However, both the -150 V and -50 V biases show a decrease in the amount of P3HT with annealing time prior to PCBM deposition, indicating more PCBM is located near the surface. Annealing the P3HT layer for 60 minutes before casting the PCBM layer causes the P3HT to form larger crystal domains near the bottom half of the bilayer. When just the P3HT layer is exposed to heat, ordering and crystallization is promoted, and these ordered domains block and limit the pathways for PCBM to diffuse to the silicon surface. More crystallization of P3HT decreases the amount of amorphous phase in the system. NR also indicates that annealing just the P3HT layer for longer times does not allow PCBM molecules to disperse to the Si substrate.

The next system studied was a 0,20, 60 minute 20/80 PCBM:P3HT annealed bilayer. The P3HT layer was thermally annealed at 150°C for 0, 20 and 60 minutes before the PCBM layer was deposited. These samples were then subsequently heated at 150°C for 15 minutes, and these are denoted as “annealed”. The NEXAFS spectra of 0, 20, and 60 minutes 20/80 PCBM:P3HT annealed bilayer is shown in Figure 3.2.3.

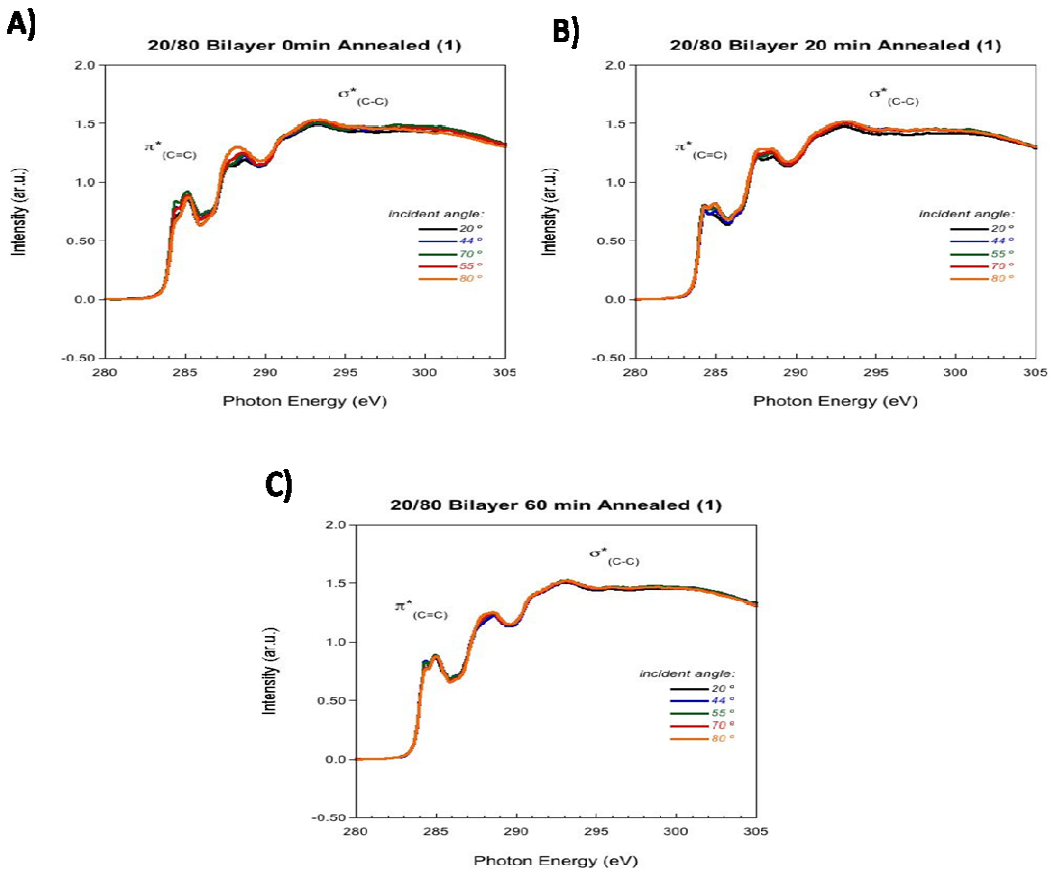

Figure 3.2.3: NEXAFS spectra of 20/80 bilayer annealed samples. The P3HT layer was first thermally annealed for A) 0 B) 20 C) 60 minutes. After depositing the PCBM on top of the preheated P3HT layer, the entire sample was annealed for 15 minutes.

The percentage of P3HT in these samples at the different depths is shown in Figure 3.2.4 as a function of P3HT layer annealing time before PCBM deposition. Initially, the 20/80 annealed samples have a higher percentage of P3HT at each depth relative to that in the 20/80 as-cast samples. Unlike the 0 minute 20/80 as-cast sample where no heat was applied to the film, annealing the 0 minute 20/80 bilayer after PCBM deposition readily disperses the PCBM molecules throughout the bulk of the film, causing more P3HT to reside at the surface of the film

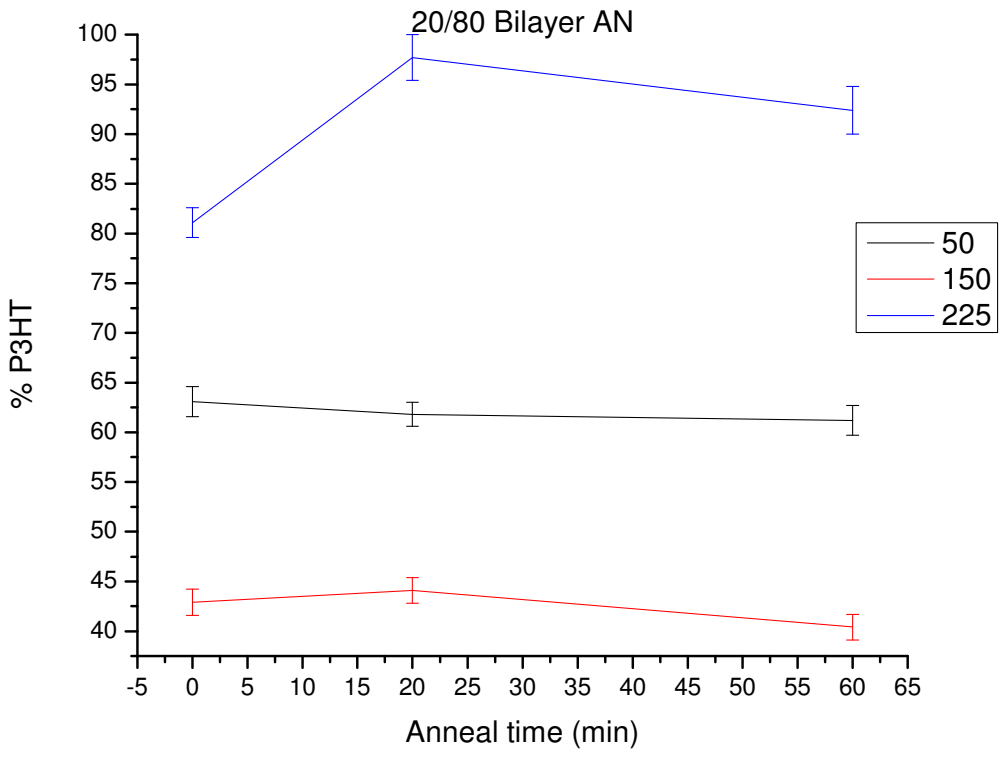

Figure 3.2.4: Percent of P3HT in a 20/80 PCBM:P3HT annealed bilayer at the top 12 nm (-50 V bias), top 9 nm (-150 V), and top 2 nm (-225 V) from the surface of the film.

After first annealing the P3HT layer for 20 minutes before casting the PCBM layer and then annealing the entire sample, an increase in the percentage of P3HT in the top 2 nm of the film (-225 V bias shown in Figure 3.2.4) indicates a P3HT rich layer forms. However, there is no change in the percentage of P3HT during this time for both the -50 V or -150 V depths. Since the top 2 nm signal is also included in the data of the top 9 nm and top 12 nm of the film, no change in the percentage of P3HT in the -50 V and -150 V indicates increase in the amount of PCBM at these depths. We have shown that in the 20 minute P3HT as-cast sample pre-heating the P3HT layer causes

crystallization of the P3HT, but still allows PCBM to migrate to occur in the amorphous region. However, annealing the entire sample for 15 minutes redistributes the PCBM back near the surface. This results in the excess PCBM at the -150 V and -50 V biases.

Annealing the P3HT layer for 60 minutes before casting the PCBM and annealing the entire sample also does not change the regions for both the -50 V and -150 V depths. Little to no change in the percentage of P3HT at the air/surface interface shows that the PCBM molecules are unable to penetrate through the highly concentrated P3HT crystalline domains in this sample. NR results correlate to these results, showing that the majority of the PCBM molecules migrate into the bulk of the film during annealing forming an amorphous region of P3HT/PCBM, but does not penetrate the narrow P3HT rich layer at the surface.

To further explore how increasing the concentration of PCBM affects the morphology of the bilayer, we examined a 40/60 PCBM:P3HT bilayer as-cast system. The NEXAFS spectra for the 0,20,60 minute 40/60 PCBM:P3HT as-cast bilayers is shown in Figure 3.2.5.The percentage of the P3HT at biases of -50 V, -150 V, and -225 V are shown in Figure 3.2.6 as a function of the P3HT layer annealing time.

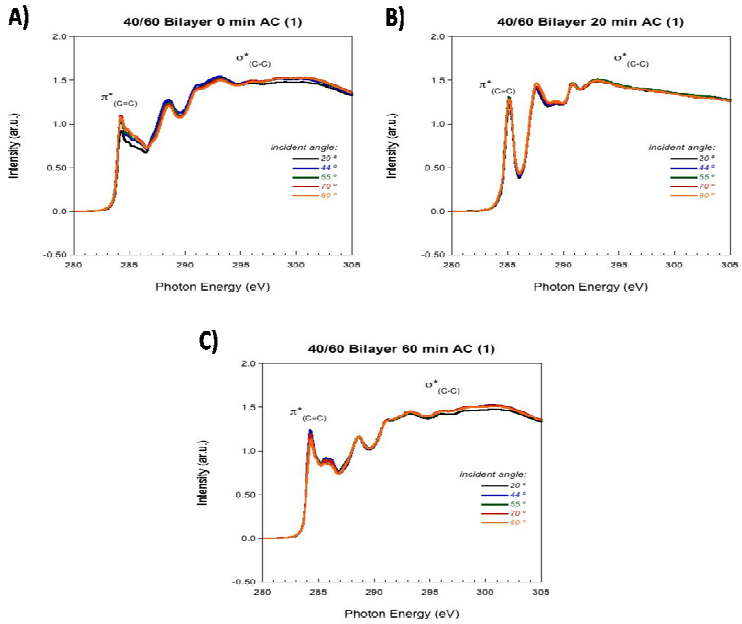

Figure 3.2.5: NEXAFS spectra of 40/60 PCBM:P3HT bilayer as-cast samples. P3HT layer was annealed for A) 0 B) 20 and C) 60 minutes prior to casting the PCBM layer.

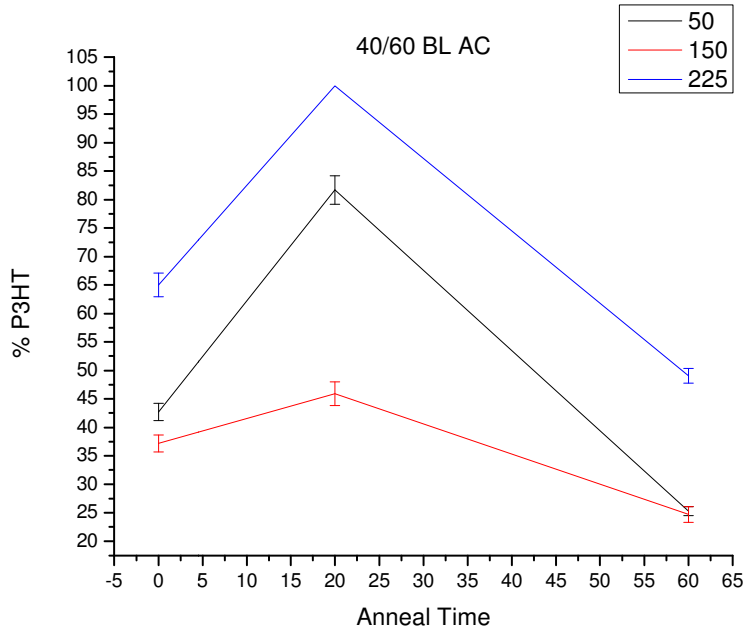

Figure 3.2.6: Percentage of P3HT of 40/60 bilayer as-cast sample at three different biases of -50, -150, and -225 V. P3HT layer was first annealed at 150 °C for 0,20, and 60 minutes then PCBM was casted on top.

Initially, the air/surface interface consists of a majority of P3HT chains (0 minute 40/60 AC sample). The percentage of P3HT in the 0 minute 40/60 as-cast sample is higher than the 0 minute 20/80 as-cast sample. By increasing the concentration of PCBM in the sample, more PCBM migrates throughout the film causing the increase in P3HT at-or-near the surface. After 20 minutes of thermally annealing the P3HT layer before casting the PCBM layer, a P3HT rich region at the air/surface interface evolves, while underneath this layer is a region containing a majority of PCBM. Preheating the P3HT layer allows P3HT to crystallize. However, unlike the miscible 20/80 sample where PCBM migrates away from the surface, the phase segregated 40/60 sample contains more PCBM near the surface. As the P3HT layer is annealed for 60 minutes before casting the PCBM layer, a dramatic decrease in the percentage of P3HT is noticed at all three depths. Annealing the P3HT layer for 60 minutes prior to casting the PCBM layer allows more P3HT to crystallize, which inhibits more PCBM from diffusing into the film during deposition of the film.

Lastly, a 40/60 annealed bilayer was investigated. The NEXAFS spectra for the 0,20, and 60 minute 40/60 PCBM:P3HT annealed bilayers is shown in Figure 3.2.7. The percentage of P3HT at a bias of -50 V, -150 V, and -225 V is shown in Figure 3.2.8 as a function of P3HT layer annealing time.

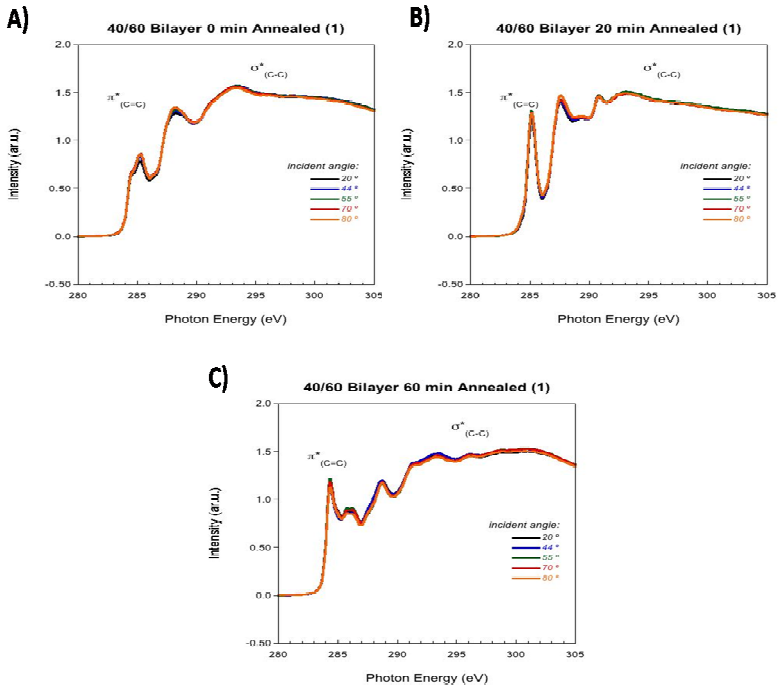

Figure 3.2.7: NEXAFS spectra of 40/60 pre-annealed bilayer. Each sample was annealed for A) 0, B) 20, and C) 60 minutes

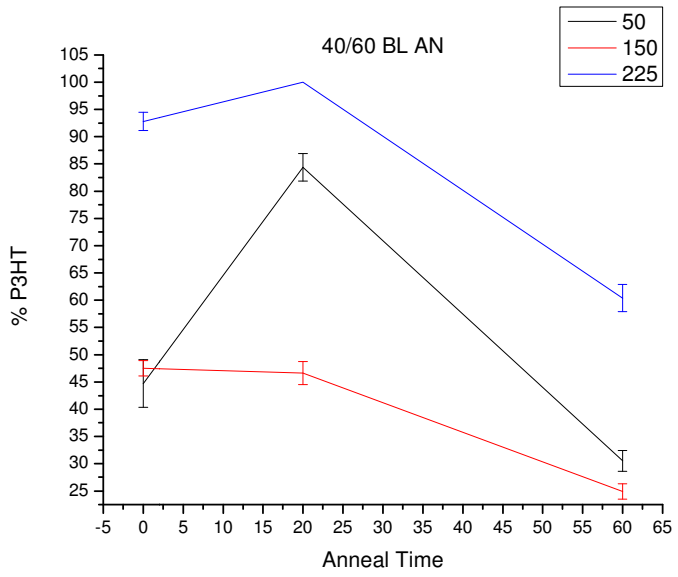

Figure 3.2.8: Percentage of P3HT of 40/60 bilayer annealed samples at 50 V (top 1-2 nm), 150 V (top 9 nm), and 225 V (top 12 nm).

Initially, a large percent of P3HT is at the top 2 nm of the film, while underneath this layer, a region containing a mixture of both PCBM and P3HT exists. After annealing the P3HT layer for 20 minutes before casting the PCBM layer and then annealing the entire sample, an increase in the P3HT is observed in the top 2 nm of the film, while the majority of the -50V and -150 V consists of PCBM. As the sample is further annealed for 60 minutes, a decrease in the amount of P3HT at all three depths occurs. Combining these observations with previously reported NR results, indicates that this sample is forming a more layered structure. The P3HT molecules are excluded from the surface, while the PCBM molecules tend to remain near the air/surface interface. A simple explanation for the interdiffusion and migration of the PCBM to the surface is entropy. Polymer chains form random coil confirmations in the bulk phase of the device. However, polymers at the air/surface interface are confined lowering the entropy of the system. PCBM traveling to the surface allows P3HT more conformational movement thus relieving the entropic penalty. Both 40/60 bilayer samples show similar trends. Thermal annealing is used to increase the crystallization of P3HT. At the same time, it drives the separation between P3HT and PCBM. Since the 40/60 system is already phase segregated, annealing the entire sample will have no affect on the overall morphology. Thus, we expect to see no change in the data for both the 40/60 as-cast and annealed samples.

3.2.2NEXAFS of P3HT:PCBM Solvent annealed Mixed Layers and Thermally annealed true Bilayers

Solvent annealing is a versatile technique which allows solvent molecules to diffuse throughout the active layer, which increases the mobility of the polymer and fullerene molecules, allowing the bulk heterojunction to evolve to a more thermodynamically stable state [64]. Two key components of the solvent annealing process are the solvent vapor pressure that the sample is exposed to and the exposure time of the sample in the solvent vapor. These two parameters are therefore controlled to explore how they affect the evolution of the morphology in these samples. NEXAFS was used to analyze the composition of a solvent annealed 1/0.8 P3HT:PCBM mixed layer at the same depths as examined in the thermal annealing study. Table 3.4.1 shows the percentage of the P3HT at various depths for two different vapor pressures (50% and 90%) and solvent annealing times. The first samples were placed in carbon disulfide (CS_2) at a SVP of 50 % and annealed for 5 and 30 seconds. The next samples were exposed to the same solvent but were placed at a SVP of 90 % and annealed for 5, 30, and 120 seconds. Annealing the sample for 5 seconds at 50 % SVP causes a large majority of P3HT chains to occupy the air surface below which resides a mixture of both P3HT and PCBM. As the samples are annealed in the solvent vapor longer, the percentage of P3HT in both the top 1-2 nm and top 12 nm increases, while the amount of PCBM increases in the top 9 nm of the film. A P3HT rich domain is forming at the surface of the film. Underneath the surface, there is a majority of PCBM molecules followed by a region containing a majority of P3HT. Our previous GIXRD and NR data also show that longer annealing times at 50 % SVP increases the P3HT crystallinity and

phase segregation[57]. These results suggest that the regions containing a majority of PCBM or P3HT are actually composed of phase segregated PCBM and crystalline P3HT instead of a completely amorphous region.

Table 3.4.1: Percentage of P3HT in a 1/0.8 P3HT:PCBM mixed layer sample solvent annealed in CS_2 at 50 % or 90 % SVP

1/0.8 P3HT:PCBM Mixture, Solvent Annealed	% P3HT		
	-50 V bias (top 10-12 nm)	-150 V bias (top 9 nm)	-225 V bias (top 1-2 nm)
5 sec @ 50 % SVP in CS_2	52.4 +-1.5	52.4 +-1.5	83.3 +- 0.7
30 sec @ 50 % SVP in CS_2	78.5 +- 1.7	51.5 +- 1.5	90.2 +- 0.9
5 sec @ 90 % SVP in CS_2	69.7 +- 1.4	46.5 +- 1.4	76.3 +- 0.6
30 sec @ 90% SVP in CS_2	71.7 +- 1.6	46.7 +- 1.3	81.6 +- 0.6
120 sec @ 90% SVP in CS_2	68.9 +- 1.7	46.5 +- 1.5	78.8 +- 0.6

Unlike the sample that was annealed at 50 % SVP, the sample that was solvent annealed at 90 % only shows changes in the amount of P3HT at the surface. At this vapor pressure, we see slightly less P3HT at the surface than previously observed in the sample

that was annealed for 5 second at 50 % SVP. As we continue to anneal at 90 % SVP, a maximum percentage of P3HT at the air surface occurs after 30 seconds. However, this value is still less than the sample that is annealed for 30 seconds at 50 % SVP. At a higher solvent vapor pressure, more PCBM molecules are dispersed underneath the surface, limiting the P3HT at the surface.

The final system that was examined monitored the surface composition of thermally annealed true bilayer samples, where the relative amount of PCBM is varied. To form the true bilayer,P3HT is cast onto a silicon wafer and floated onto the surface of high purity water, which was then captured by a PCBM coated Si wafer. The samples that were studied contained volume fractions of 11 %, 25 %, 30 %, and 37 % PCBM and were thermally annealed at 150 °C for 60 minutes. The composition of the layers near the surface of the film were then determined from the NEXAFS data and are presented in Table 3.4.2. This table shows that as the loading of PCBM increases in the sample, the amount of P3HT at each depth decreases. By increasing the amount PCBM into the system, more PCBM is able to diffuse from the PCBM layer to the P3HT layer.

Table 3.4.2: Percentage of P3HT in thermally annealed PCBM:P3HTbilayers with a loading of 11 % PCBM, 25 % PCBM, 30 % PCBM, and 37 % PCBM

PCBM:P3HT bilayer, thermally annealed @ 150 ° C	% P3HT		
	-50 V (top 10-12 nm)	-150 V (top 9 nm)	-225 V (top 1-2 nm)
11 % PCBM	92.3 +- 0.8	56.1 +- 1.4	92.3 +- 1.1
25 % PCBM	88.1 +- 0.9	55 +- 1.4	88 +- 2.9
30 % PCBM	86.1 +- 1.1	54.9 +- 1.3	87.4 +- 1.4
37 % PCBM	83.7 +- 0.8	50.5 +- 1.6	81.2 +- 1.3

CHAPTER IV
PHYSICAL PROPERTIES OF THIN POLYMER FILMS

4.1 Young's Modulus

Thin film polymers are important systems in the fields of pharmaceutical, medical, and aerospace industries. To help improve these technologies, a better understanding of how the polymers respond to an applied stress is necessary. Deformities that may occur during production or from an externally applied stress can cause slight tears or complete malfunction of the polymer. Therefore, the physical properties of these thin films must be accurately characterized insure that manufacturers can control the quality of the materials. However, conventional mechanical testing devices do not have the sensitivity to accurately determine the physical properties of these thin films [65, 66]. Scanning probe microscopy has been used to measure the moduli of polymer films, however, uncertainty in the contact area and/or tip size limits the accuracy of these types of measurements [67]. Providing a cheap, reliable, simple, and high-throughput method to determine the physical properties of thin films is essential in expanding the technologies and uses of thin film polymers.

One important physical property of a polymer thin film is its, Young's modulus, a measure of its rigidity. Monitoring the phenomenon of wrinkling thin films as a method to monitor their rigidity has been explored [65, 66, 68]. Hydrophobic polymers such as polystyrene (PS) repel water allowing their thin films to float when placed on top of water. By introducing a droplet of water on the surface of the thin film floating in an aqueous environment, the film wrinkles, which is caused by the deformation of the film

due to the weight of the water droplet. For instance, Huang et al. correlated the characteristics of the wrinkling process, such as the number of wrinkles (N) and the length of the wrinkles (L), to the Young's modulus of the film. This provides a method to accurately determine the mechanical properties of the thin film using only a low magnification microscope to image the wrinkling. They showed that the length of the wrinkles (L) is related to the modulus of the thin film by:

– (4.1)

where E is Young's modulus, is the radius of the droplet, h is the thickness of the film, is the water surface tension,72 mN/m, and C_L is a constant (0.031). The constant C_L was determined from the dependence of L on $ah^{1/2}$, shown in Figure 4.1.

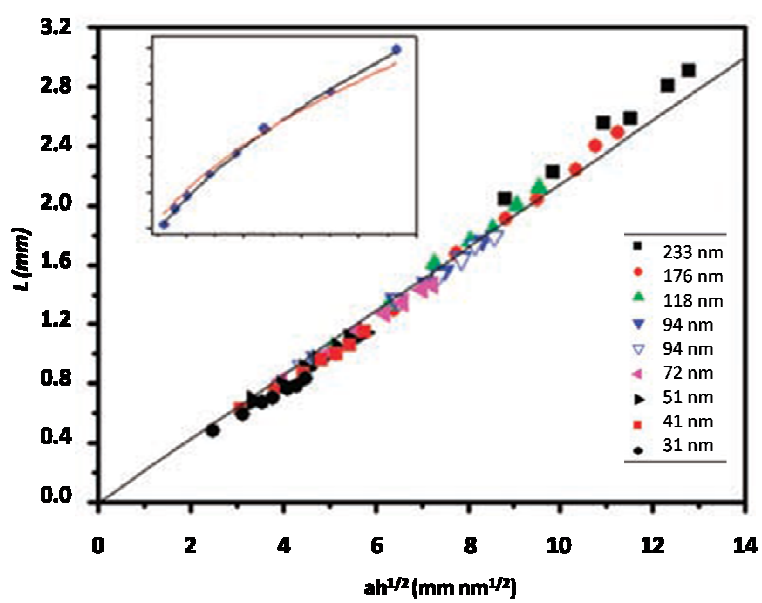

Figure 4.1: Graph plotting the length of the wrinkles (L) as a function of the variable $ah^{1/2}$, where a is the radius of the droplet and h is the thickness of the film. 65]

4.2 Determining Diffusion Coefficients of Gases in Polymer Thin Films

When using polymers in drug delivery, the amount of drug released and the time interval at which it is released are important factors that need to be considered. Both of these factors concern the diffusion of a small molecule through the polymer. This and other technologies suggest that developing a simple, cheap method to determine the diffusion coefficient of a small molecule in a polymeric thin film is needed.

To realize this, a bubble of a gas is placed underneath a polymer thin film and allowed to slowly diffuse through the film. By measuring the radius of the bubble, we can calculate the volume of the bubble ,$V=\pi r^3$, assuming the bubble is a complete sphere. The change in bubble volume due to this diffusion is shown in Figure 4.2.1.

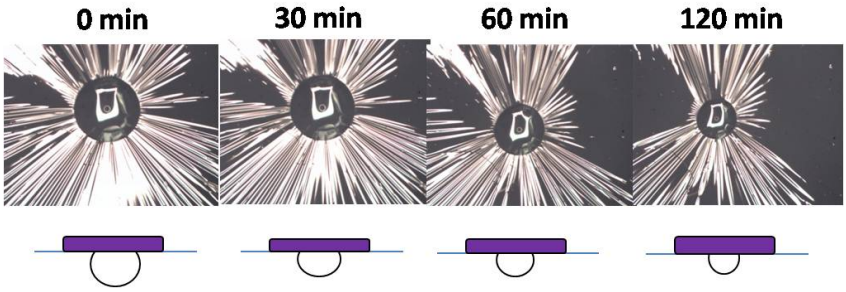

Figure 4.2.1: A timeline of the diffusion of a gas through a thin film of polystyrene.

The diffusion coefficient of the gas in the thin polymer film is calculated by graphing the flux of gas diffused (Q_t) as a function of time, as shown in Figure 4.2.2. Fitting the plotted data to a line gives a time lag of θ, which denotes the time it takes for the gas to diffuse through the film. Thus, the diffusion coefficient of the gas in the polymer film can be calculated Equation 4.2:

$$D = \frac{l^2}{6\Theta} \qquad (4.2)$$

where l is the thickness of the film and Θ is the time lag determined from the experimental data.

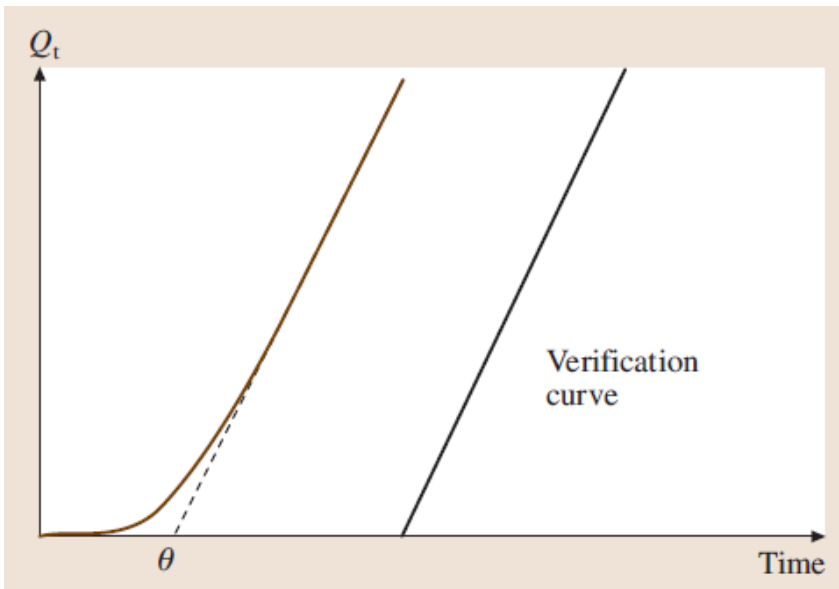

Figure 4.2.2: A typical curve for the amount of diffused gas (Qt) versus time graph [65]. θ is determined by the linear best fit line.

In this research program, the validity of this technique to accurately monitor the diffusion of a gas in a polymer thin film will be examined. To realize this goal, the diffusion coefficient of oxygen, argon, nitrogen, and air in polystyrene will be determined. These results will then be interpreted to test the validity of this technique to accurately monitor the diffusion coefficient of small molecules in polymer thin films. It is the overall goal of this research program to develop a simple, inexpensive, reliable, and high-throughput method to determine the physical properties of polymeric thin films.

4.3 Experimental Methods

4.3.1 Preparation of polystyrene thin films

Polystyrene (PS) thin films were fabricated by spin-coating solutions of polystyrene (M_w=106,000 M_n=100,000) purchased from Polymer Source Inc. in HPLC grade toluene purchased from Fischer Scientific. To further purify toluene, a 0.45 µm microporesyringe filter was used. A two percent weight/weight solution of polystyrene and toluene was heated overnight at 55 °C. To eliminate undissolved polystyrene, the solution was purified by filtering with a 0.45 µm syringe filter. Si wafers were cleaned by sonication in DI water, acetone, and isopropyl alcohol. A uniform SiO layer was established by UV/Ozone treatment for 20 minutes. Before depositing the polystyrene solution on the wafer, a layer of nanopure water was spun on the wafer at 1800 rpm for 30 seconds. Next, a thin film of polystyrene was deposited on top of the wafer by spin coating at 1000 rpm for 90 seconds. The thin films were placed in a vacuum oven for 30 minutes to ensure all solvent had evaporated. Before floating the film, a razor blade was used to remove excess polystyrene from the sides of the substrate. The corner of the film was slowly placed into a container filled with nanopure water. Surface tension between the film and water causes the film and Si substrate. The substrate was continuously lowered into the water allowing the entire film to detach from the substrate, creating a floating film of polystyrene.

4.3.2 Ellipsometry

To determine the thickness of the PS thin films, an ellipsometer (DRE EL X-02C) was used. Ellipsometry is an accurate, sensitive optical technique useful in determining the roughness or thickness of thin films. An illustration of the components of an ellipsometer is shown in Figure 4.3.1. Typically, a laser is used as a light source. When the laser beam hits the surface of the sample, it is reflected and collected by the detector. The incidence angle (θ) was set to 70 degrees. The laser beam reflects off the sample at the same angle as the incidence angle and is received by the detector, which is analyzed to determine the thickness. The sensitivity of the amplifier of the ellipsometer was adjusted with the potentiometer at the receiver unit to approximately 75- 80 %. The rest intensity in the room was measured to eliminate any ambient light reaching the detector. The sample was aligned to ensure accurate thicknesses. A simulation model based on the thickness and refractive index of the Si substrate and PS was used to calculate the thickness of the film.

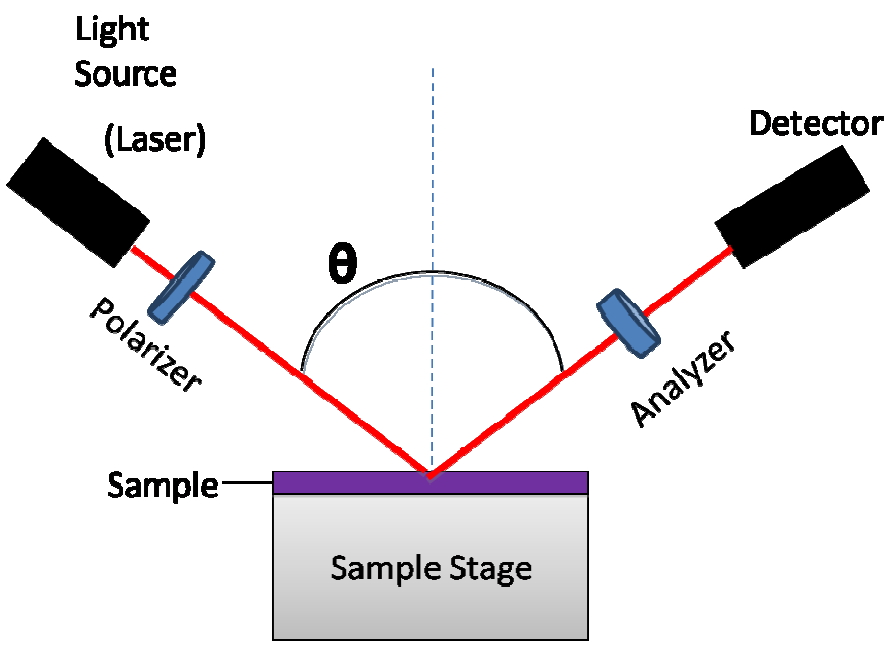

Figure 4.3.1: Illustration of Ellipsometer apparatus.

4.4 Results and Discussion

4.4.1 Determining Young's Modulus of thin polymer films

To determine the Young's modulus of a thin PS film, a syringe was used to place an approximately 0.1 mL droplet of water on top of a 110.5 nm thick polystyrene film. The wrinkling of the film is shown in Figure 4.4.1. Equation 4.1 then provides Young's modulus (E). A list of parameters to determine Young's modulus is shown in Table 4.4.1, from which the Young's modulus was determined to be 5.5 GPa. Literature values of the modulus of bulk polystyrene are reported to be between 3.0 and 3.6 GPa [68]. A slight difference of the modulus of the thin film from that of the bulk is not unexpected however, this deviation is higher than expected.

Table 4.4.1: Parameters used to determine the elastic modulus. Young's modulus for polystyrene was calculated to be 5.5 GPa. The literary value was reported to be 3.0- 3.6 GPa [69].

N	L (mm)	□ (mm)	□ (nm)	C_L	γ (mN/m)	E (GPa)
80	3.8	1.28	110.5	0.031	72	5.5

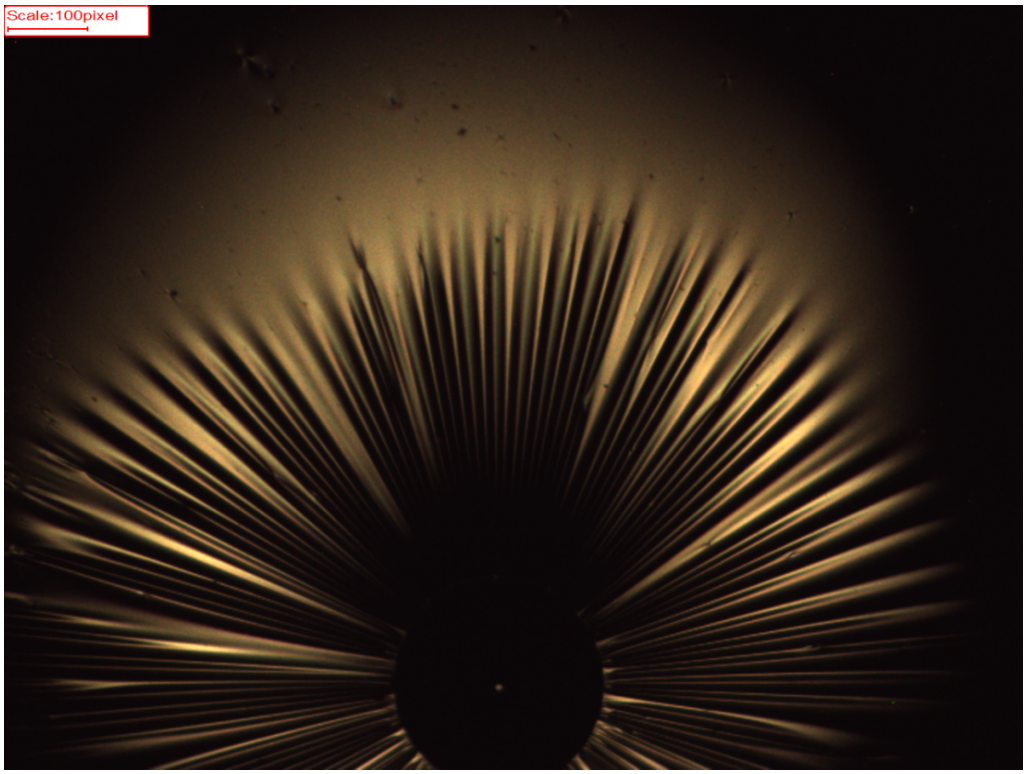

Figure 4.4.1: Wrinkling of a thin film of polystyrene by placing a droplet of water on top of a film in an aqueous environment. The scale is 100 pixels = 1 mm.Using Equation 4.1, Young's modulus was calculated to be 5.5GPa.

Since the wrinkling pattern is characterized by the number and length of the wrinkles, it is important to explore the accuracy of characterizing these two physical observations to explain the variation of our results from those reported in the literature.

First, we inspected the number of wrinkles (N). Huang established a correlation between N and the radius of the droplet and the thickness of the film, as shown in Figure 4.4.2, N ~ $a^{1/2}h^{-3/4}$. By using our measured drop radius (a) of 1.28 mm and 110.5 nm film thickness (h), we obtain a value for $a^{1/2}h^{-3/4}$ to be 0.033 $mm^{1/2}nm^{-3/4}$. According to the data in Figure 4.4.2, this value corresponds to approximately 75 wrinkles, where analysis of our sample indicates that there are 80 wrinkles in this film. Thus, the characteristics of our wrinkling experiment are concurrent with the findings of Huang et al.

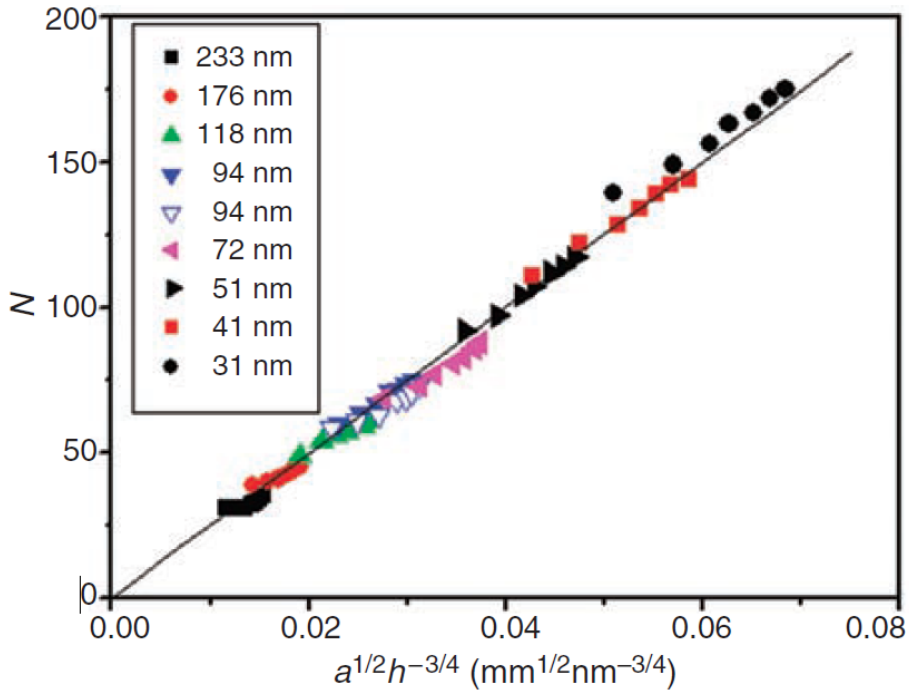

Figure 4.4.2: Graph relating the number of wrinkles (N) as a function of the radius of the droplet and thickness of the film [65].

Next, we critically evaluate the length of the wrinkle. The lengths of the wrinkles were measured from the edge of the water droplet to the end of wrinkle, where an average wrinkle length of 3.8 mm was measured. The length of the wrinkles was

correlated to the radius of the droplet and thickness of the film, $ah^{1/2}$, as shown in Figure 4.1. Using the radius and thickness of the film studied in our lab (Table 4.4.1), the value of $ah^{1/2}$ was determined to be 13.46 $mmnm^{1/2}$. From this relationship, Huang's data suggest that the length of the wrinkle should be 2.8 mm. The difference in the length of the wrinkle may explain our high Young's modulus.

The reason for this discrepancy may be elucidated by independently evaluating the value of C_L to test its universality. This is ongoing in our lab, however, our goal in replicating these results was to develop a basic knowledge of the floating process using thin films and creating a setup to visualize these films, which were both achieved. Our real focus is varying this setup to achieve diffusion coefficients of gases through thin films.

4.4.2 Determining the Diffusion Coefficients of Gases through Thin Polymer Films

By slightly varying the method used to determine the Young's modulus of a thin polymer film, a method to determine the diffusion coefficient of gases through a thin film of polystyrene is sought. Initially, a known volume of gas was placed underneath the floating polystyrene film and an image was taken. After each 60 second interval, a sequential image was collected. The radius of the bubble was measured for each image. Assuming the bubble of gas is a sphere, the volume of the bubble($V=\pi r^3$) is calculated. The change in volume of an air bubble was therefore monitored and is shown in Figure 4.4.1. Inspection of this curve shows that there are two distinct changes in the volume

change with time, indicating the diffusion of two different gas components. We interpret this to be the diffusion of the major components of air, oxygen and nitrogen.

This makes sense, as previous research has shown a relationship between the size and shape of gas molecules on the diffusion rates of each gas [70]. Since O_2 molecules are smaller than N_2, the first volume change should be the diffusion of oxygen and the second, that of nitrogen. By fitting this data to a linear fit, the time lapse (θ) for the diffusion of each gas is calculated by the x-intercept of the linear fit line, from which the diffusion coefficients are determined. Figure 1A and Figure 2A (Appendix) shows the fits used to complete the calculation. This analysis provides values of 1.64×10^{-11} and 3.17×10^{-13} cm^2/s for the diffusion coefficients of the two gases. Literature values for the diffusion coefficient oxygen and nitrogen in polystyrene are 9.1×10^{-8} and 2.3×10^{-8} cm^2/s respectively [71]. While a small difference from literature values may be expected due to some of the gas diffusing into the surrounding water, this large difference between our results and the literature values is concerning. It is also interesting to note that not all of the bubble diffused through the film, which was unexpected. To more fully understand this behavior, the diffusion of different gases through PS were examined.

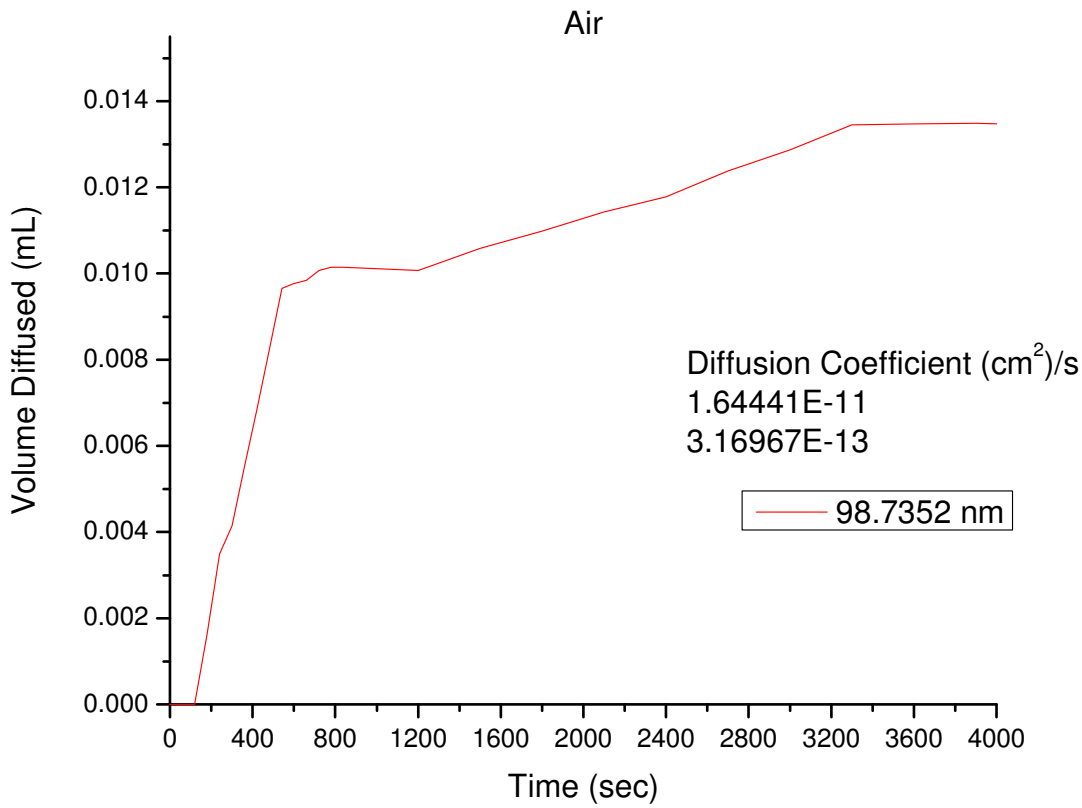

Figure 4.4.1: Graph of volume of air diffused (mL) as a function of time (sec). Two distinct trends were noticed. The diffusion coefficients were determined to be 1.64 x 10^{-11} and 3.17 x 10^{-13} cm^2/s.

To further test our results for the diffusion of air, we investigated the diffusion of pure O_2 and pure N_2. The change in the volume of the oxygen bubble as a function of time is shown in Figure 4.4.2, from which a diffusion coefficient of 1.20 x 10^{-13} cm^2/s was determined. Figure 3A (Appendix) shows the linear fit used to determine the time lag (θ). This value is an order of magnitude different that the value determined from characterizing the diffusion of air through PS. sample. The slight difference may be caused by imperfections in the polystyrene. Research has shown glassy polymers, such as

polystyrene, have long relaxation times [71]. This slower movement of the chains will allow gases to be trapped in small pockets between polymer chains decreasing the diffusion through the film. This would account for the slight difference that was observed. However, this variation does not account for the difference between our characterization and the literature value.

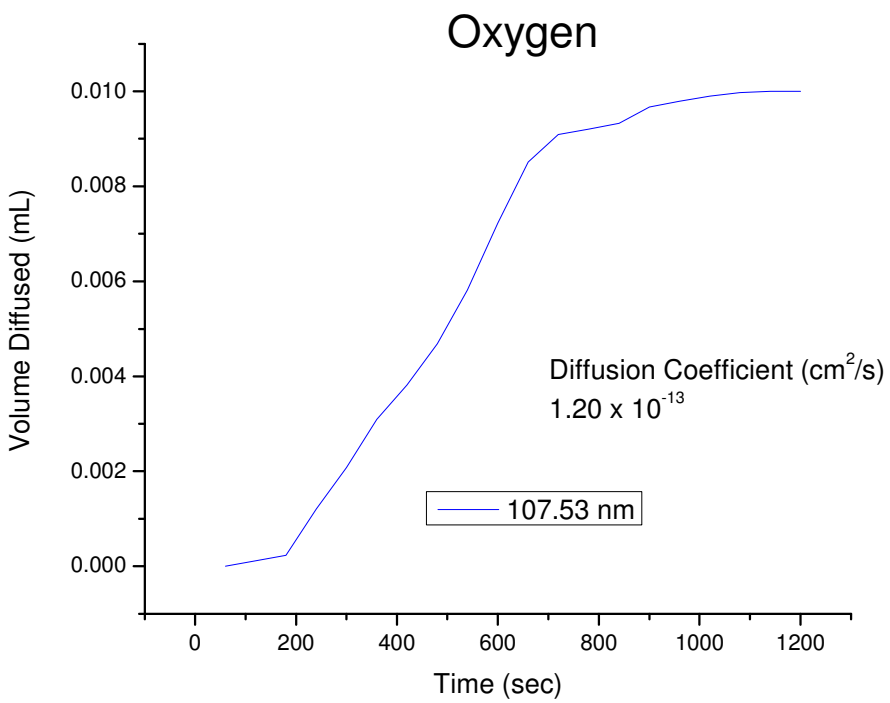

Figure 4.4.2: Graph of volume of oxygen diffused as a function of time. The diffusion coefficient was determined to be 1.20 x 10^{-13} cm^2/s.

Next, the diffusion of pure nitrogen through a polystyrene film was monitored. To further test this process, the initial volume of placed underneath the film was varied. Figure 6.6.3 shows the diffusion of nitrogen through the PS think film when starting with a 0.015 mL (red line) and 0.01 mL (black line) bubble. The linear fit used to determine

the time lag is shown in the appendix (Figure 4A and Figure 5A).These data translate to diffusion coefficients of 6.72 x 10^{-14} and 6.40 x 10^{-14} cm^2/s , verifying that the initial volume of the bubble does not affect the measured diffusion coefficient through the film.

Unfortunately, there remains a difference in these experimentally determined diffusion coefficients and the diffusion coefficients determined by analysis of the diffusion of air through the thin films. One explanation in these differences may relate to the precise structure of the thin film. In the air sample the smaller permeant (i.e. oxygen), which diffuses through the film first, may plasticize the film [71]. This may alter the structure, allowing for a faster diffusion of the second component, causing a difference in the observed values.

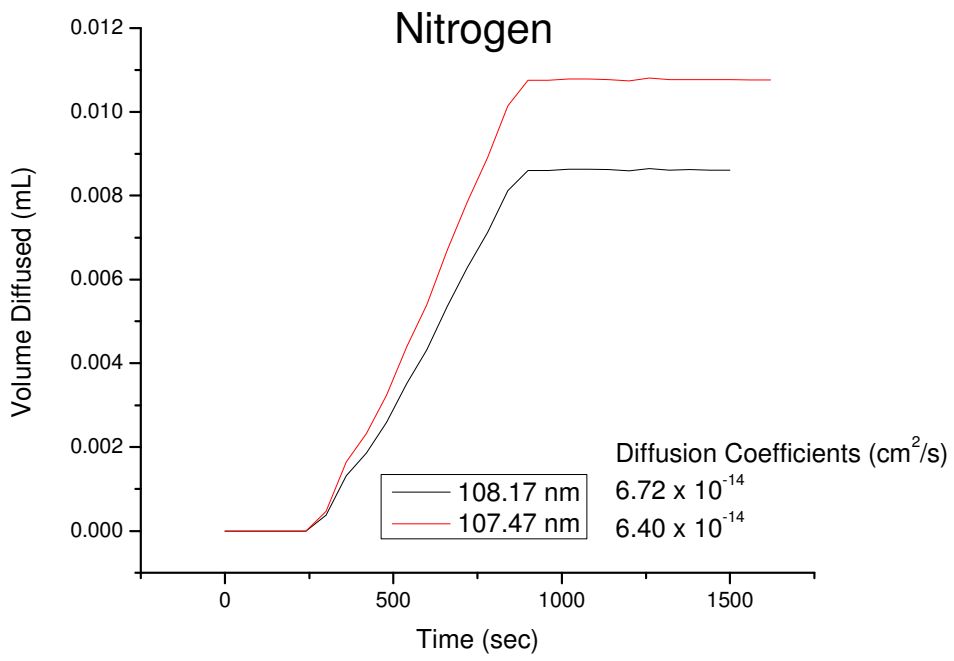

Figure 4.4.3: Graph of volume of N_2 gas diffused as a function of time. Diffusion coefficients were determined to be 6.72 x 10^{-14} (108.17 nm film) and 6.40 x 10^{-14} cm^2/s (107.47 nm film).

The last experiment was performed using argon. Argon gas is smaller in size than the diatomic N_2 gas but larger than O_2, therefore, a diffusion coefficient that is intermediate between that of oxygen and nitrogen is expected. The graph that monitors the diffusion of argon gas through the PS thin film as a function of time is shown in Figure 4.4.4. Analysis of this data(Appendix: Figure 6A) results in a diffusion coefficient of 1.14 x 10^{-13} cm^2/s, a value that is between the diffusion coefficients of oxygen and nitrogen. However, the value is once much smaller than the literature value of 4.1 x 10^{-8} cm^2/s [71].

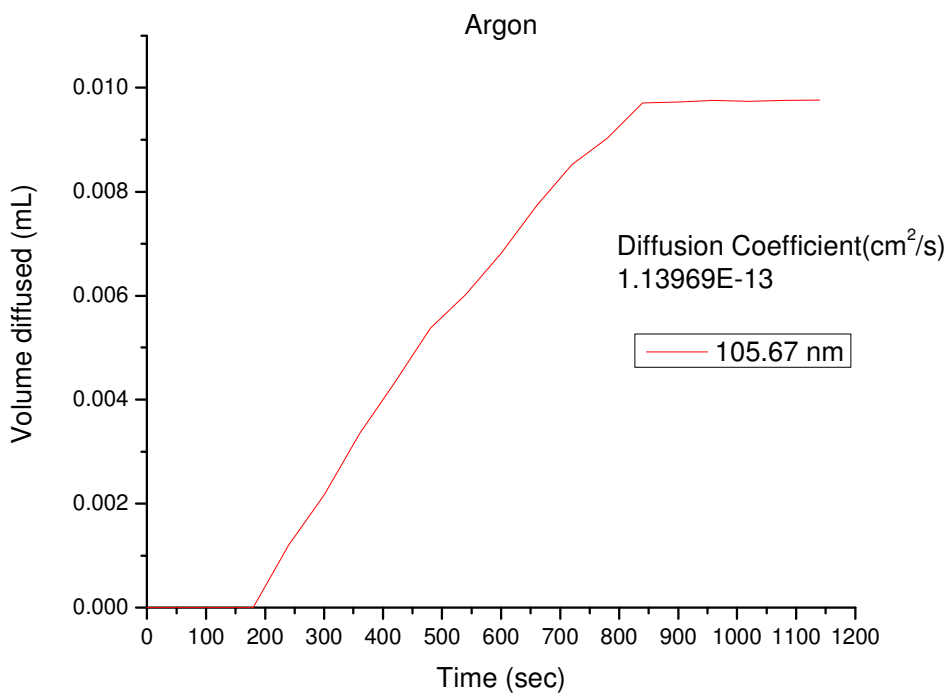

Figure4.4.4: Graph of diffusion of argon gas as a function of time. The diffusion coefficient was calculated to be 1.14 x 10^{-13} cm^2/s.

The question now arises what are we actually measuring? If not diffusion or a process related to it, how are we able to selectively separate nitrogen and oxygen molecules? These questions may be answered by exploring the relationship between diffusion and permeability.

Permeation of small molecules through polymers was first observed over a century ago. In 1866, Thomas Graham developed a mechanism to explain the diffusion of a gas through a membrane known as the solution-diffusion process [70]. An illustration of the process is shown in Figure 4.4.5. In the first step, small permeants (i.e. gas molecules) travel from upstream into the polymer matrix. An increase in the pressure or concentration of the gas in the polymer film is the driving force behind the movement into the polymer. Next, the molecules diffuse through the polymer. This diffusion rate is different for every polymer. Chain packing, plasticization, and bulkiness of the sides groups affect how fast molecules can move through the film [72]. Once the molecules reach the surface of the polymer membrane, desorption of the molecules from the polymer surface to the downstream region occurs. To make this process feasible, it is assumed that the system follows the free volume theory. This theory postulates that a polymer matrix contains three distinct components:

1. A volume occupied by the polymer
2. A small interstitial free volume
3. A unoccupied excess free volume

This excess free volume allows gas molecules to diffuse through the polymer. Differences in transport of gas molecule through rubbery and glassy polymers have been well investigated [70-72]. Since glassy polymers are not a true equilibrium, diffuse

through the film is more difficult than rubbery polymers. Glassy polymers are also hard and brittle, which restricts the mobility and rotation of the chain along the chain axis, which may make the diffusion of a gas possible. The longer relaxation times increase the time gas molecules stay in the matrix longer causing slower permeability.

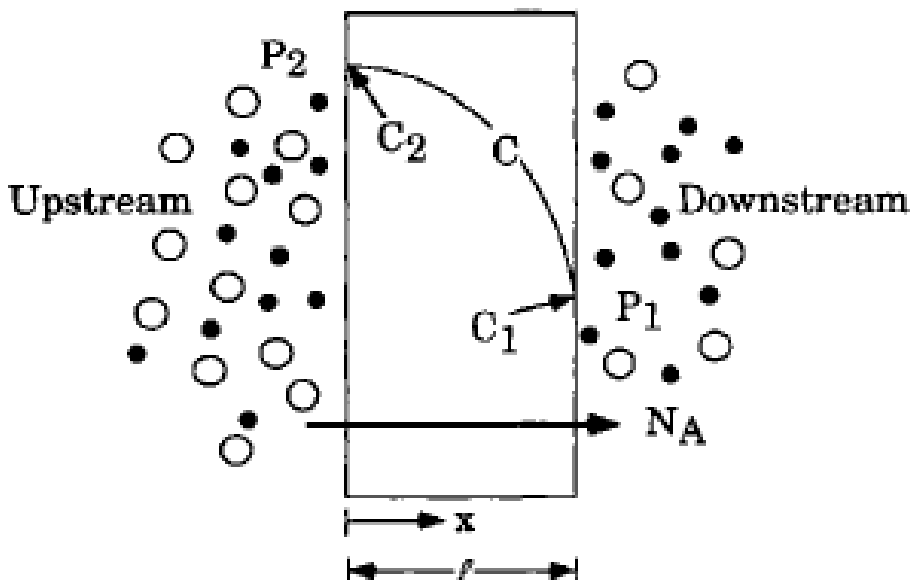

Figure 4.4.5: Illustration of transport of gas molecules across a membrane [72].

The Permeability (P) of a polymer film is related to diffusion and solubility by:

$$P = DS \quad (4.4.1)$$

where D is the diffusion coefficient of the gas through the polymer and S is the solubility of the polymer matrix. If we can determine the permeability of gas through a polymer, we can use the literary value for the solubility to calculate the diffusion coefficient. The permeability coefficient (P) for gases through a polymer can be calculated using the equation:

$$q = Pp_1 \mathrm{A}(\mathrm{t} - \theta)/\mathrm{l} \quad (4.4.2)$$

where q is the rate of transport per unit area, p_1 is the partial pressure of the upstream region (assuming the downstream pressure is 0), A is the area of permeation, t is the time, θ is the time lag of the permeation, and l is the thickness of the film [73]. In our experiments, the bubble of gas below the film creates pressure. As long as the pressure of the bubble is greater than the pressure exerted from the top of the film, permeation of the gas through the film will occur. This explains why not all of the volume of the bubble was able to diffuse. Future experiments are therefore needed to correlate the permeation of the gas through the film to test whether these experiments accurately characterize the diffusion coefficients of gases in polymer thin films, or if additional processes occur in this experiment that are not accounted for.

CHAPTER VII
CONCLUSION AND FUTURE WORK

The miscibility of the system clearly affects the morphology of a solvent annealed PCBM:P3HT bilayer. The crystallinity of P3HT in a miscible 10/90 PCBM:P3HT bilayer decreases as the solvent annealing time increases. However, there is an increase in the average crystal size at longer annealing times. At low concentrations, PCBM acts like a solvent molecule, dissolving smaller P3HT crystals. Increasing the PCBM to slightly below the miscibility limit in the 20/80 sample led to an increase in the crystallinity and crystal size. Smaller crystals of P3HT are being dissolved by both PCBM and ODCB molecules, while larger crystals are continuing to grow. Lastly, a 40/60 bilayer above the miscibility limit was explored. Little to no change in the crystallinity and crystal size occurs as we solvent anneal the sample. These results show that, in a phase segregated system,larger P3HT crystalline domains are dissolving as P3HT chains in smaller domains continue to stack creating larger crystals.

We compared the crystallinity results to Raman "aggregation" to determine if there is a correlation between the two. By directly comparing the two, we see discrepancies between the results. We suggest there is an intermediate ordering between the highly ordered crystals and the disordered amorphous regions. This ordering is referred to as a "condos crystal", where the structure permits liquid-like ordering while retaining orientation order. To quantify the amount of this intermediately ordered structure that exists in a sample, we introduce a qualitative measure of the crystalline surface area, which incorporates the volume of the crystal, as measured by the polymer

crystallinity and a characteristic length scale of the crystal, the crystal size. Surface area correlates to the Raman "aggregated" species.

Next, we used NEXAFS to explore the affects preheating a P3HT layer and annealing the entire sample have on 20/80 and 40/60 PCBM:P3HT bilayers. Initially, annealing the entire sample leads to more P3HT appearing at-or-near the surface for the 0 minute 20/80 and 40/60 annealed samples compared to the 0 minute 20/80 and 40/60 as-cast samples. Although pre-heating the P3HT layer for 20 minutes prior to casting the PCBM layer induces crystallization of the P3HT for both the 20/80 and 40/60 as-cast films, there is still an amorphous region at the bulk interface. This amorphous region allows PCBM to migrate away from the surface. Annealing the P3HT layer for 60 minutes prior to casting the PCBM layer for the 20/80 and 40/60 as-cast films causes more crystallization of the P3HT decreases the amount of amorphous phase in the system, inhibiting the PCBM molecule to migrate downward. Annealing the entire sample for 15 minutes redistributes the PCBM back near the surface. However, the 40/60 sample is already phase segregated and annealing the entire sample does not affect the morphology.

We also used NEXAFS to explore the affects of solvent vapor pressure and solvent exposure time on a 1/0.8 P3HT:PCBM mixed layer. Annealing the mixed layer in CS_2 at 50 % SVP for 60 seconds compared to 5 seconds increases the P3HT at the surface and to a depth of 10-12 nm. A P3HT rich layer is forming at the surface, while an regions consisting of mostly PCBM followed by mostly P3HT are underneath. Solvent annealing for 30 seconds at 90 % SVP only shows an increase in P3HT at the air/surface

interface. We concluded that at the higher 90 % SVP, more PCBM molecules migrate to the surface region limiting the amount of P3HT at the surface.

The final NEXAFS experiments examined the surface composition of thermally annealed true bilayer samples, where the relative amount of PCBM is varied from 11 %, 25 %, 30 %, and 37 %. By increasing the amount PCBM into the system, more PCBM is able to diffuse from the PCBM layer to the P3HT layer..

The last experiments used a low cost, simple method to determine different physical properties of thin film polymers. We determined the Young's modulus of a thin film of polystyrene to be 5.5 GPa. This value does not compare to the literary value of 3.0-3.6 GPa. Since the wrinkling pattern is characterized by thenumber and length of the wrinkles, we explored these two physical observations to explain the variation of our results from those reported in the literature. We measured 80 wrinkles in our film, which is concurrent with the results of Huang et al. The average wrinkle length was measured to be 3.8 mm. This length does not agree with Huang et al. reported for the wrinkle length created with similar conditions (2.8 mm). The reason for this discrepancy may be due to the value of C_L. Future research needs to be conducted to independently evaluating the value of C_L to test its universality.

We used a similar methodology to determine the diffusion coefficients of air, oxygen, nitrogen, and argon through the polystyrene thin film. The volume change of air showed two distinct trends. We concluded these to be the major components of air, oxygen and nitrogen. However, the calculated diffusion coefficients of oxygen and nitrogen in air were not accurate with literature values. We were not able to accurately determine the diffusion coefficients of oxygen, nitrogen, or argon. However, we proposed

the experimental set up used could possibly determine the permeability of gases through thin film polymers. If we can measure the permeability of gases through thin films, we can also determine the diffusion coefficients of gases. Future experiments are needed to test for the permeation of the gases through the thin polymer film.

REFERENCES

1. U.S. Energy Information Administration, *International Energy Outlook 2009*, http://www.eia.doe.gov/oiaf/ieo/index.html, 2009.
2. Tao, M. (2008). Inorganic photovoltaic solar cells: silicon and beyond. *The Electrochemical Society Interface*, *17*(4), 30-35.
3. Peet, J., Heeger, A. J., & Bazan, G. C. (2009). "Plastic" solar cells: Self-assembly of bulk heterojunction nanomaterials by spontaneous phase separation. *Accounts of chemical research*, *42*(11), 1700-1708.
4. Kim, J. Y., Lee, K., Coates, N. E., Moses, D., Nguyen, T. Q., Dante, M., &Heeger, A. J. (2007). Efficient tandem polymer solar cells fabricated by all-solution processing. *Science*, *317*(5835), 222-225.
5. Chen, F. C., Ko, C. J., Wu, J. L., & Chen, W. C. (2010). Morphological study of P3HT: PCBM blend films prepared through solvent annealing for solar cell applications. *Solar Energy Materials and Solar Cells*, *94*(12), 2426-2430.
6. Chen, J., & Cao, Y. (2009). Development of novel conjugated donor polymers for high-efficiency bulk-heterojunction photovoltaic devices. *Accounts of chemical research*, *42*(11), 1709-1718.
7. Treat, N. D., Brady, M. A., Smith, G., Toney, M. F., Kramer, E. J., Hawker, C. J., & Chabinyc, M. L. (2011). Interdiffusion of PCBM and P3HT reveals miscibility in a photovoltaically active blend. *Advanced Energy Materials*, *1*(1), 82-89.
8. Rowell, M. W., Topinka, M. A., McGehee, M. D., Prall, H. J., Dennler, G., Sariciftci, N. S., ... &Gruner, G. (2006). Organic solar cells with carbon nanotube network electrodes. *Applied Physics Letters*, *88*(23), 233506.
9. Na, S. I., Kim, S. S., Jo, J., & Kim, D. Y. (2008). Efficient and Flexible ITO-Free Organic Solar Cells Using Highly Conductive Polymer Anodes. *Advanced Materials*, *20*(21), 4061-4067.
10. Wu, J., Becerril, H. A., Bao, Z., Liu, Z., Chen, Y., &Peumans, P. (2008). Organic solar cells with solution-processed graphene transparent electrodes. *Applied Physics Letters*, *92*(26), 263302.

11. Verploegen, E., Mondal, R., Bettinger, C. J., Sok, S., Toney, M. F., &Bao, Z. (2010). Effects of thermal annealing upon the morphology of polymer–fullerene blends. *Advanced Functional Materials*, *20*(20), 3519-3529.
12. Lee, S. T., Gao, Z. Q., & Hung, L. S. (1999). Metal diffusion from electrodes in organic light-emitting diodes. *Applied Physics Letters*, *75*(10), 1404-1406.
13. Tang, J. X., Zhou, Y. C., Liu, Z. T., Lee, C. S., & Lee, S. T. (2008). Interfacial electronic structures in an organic double-heterostructure photovoltaic cell. *Applied Physics Letters*, *93*(4), 043512-043512.
14. Eo, Y. S., Rhee, H. W., Chin, B. D., & Yu, J. W. (2009). Influence of metal cathode for organic photovoltaic device performance. *Synthetic Metals*, *159*(17), 1910-1913.
15. Steim, R., Kogler, F. R., &Brabec, C. J. (2010). Interface materials for organic solar cells. *Journal of Materials Chemistry*, *20*(13), 2499-2512.
16. Li, G., Zhu, R., & Yang, Y. (2012). Polymer solar cells. *Nature Photonics*, *6*(3), 153-161.
17. Heremans, P., Cheyns, D., & Rand, B. P. (2009). Strategies for increasing the efficiency of heterojunction organic solar cells: material selection and device architecture. *Accounts of chemical research*, *42*(11), 1740-1747.
18. Liu, F., Gu, Y., Jung, J. W., Jo, W. H., & Russell, T. P. (2012). On the morphology of polymer-based photovoltaics. *Journal of Polymer Science Part B: Polymer Physics*, *50*(15), 1018-1044.
19. Hu, Z., Zhang, J., Hao, Z., & Zhao, Y. (2011). Influence of doped PEDOT: PSS on the performance of polymer solar cells. *Solar Energy Materials and Solar Cells*, *95*(10), 2763-2767.
20. Hou, J., Chen, H. Y., Zhang, S., Chen, R. I., Yang, Y., Wu, Y., & Li, G. (2009). Synthesis of a low band gap polymer and its application in highly efficient polymer solar cells. *Journal of the American Chemical Society*, *131*(43), 15586-15587.

21. Chen, H. Y., Hou, J., Zhang, S., Liang, Y., Yang, G., Yang, Y., ... & Li, G. (2009). Polymer solar cells with enhanced open-circuit voltage and efficiency. *Nature Photonics*, *3*(11), 649-653.
22. Price, S. C., Stuart, A. C., Yang, L. Q., Zhou, H. X. & You, W. Fluorine substituted conjugated polymer of medium band gap yields 7% efficiency in polymer–fullerene solar cells. *J. Am. Chem. Soc.* **133,** 4625–4631 (2011).
23. Zhou, H., Yang, L., Stuart, A. C., Price, S. C., Liu, S., & You, W. (2011). Development of fluorinated benzothiadiazole as a structural unit for a polymer solar cell of 7% efficiency. *AngewandteChemie*, *123*(13), 3051-3054.
24. Chen, D., Liu, F., Wang, C., Nakahara, A., & Russell, T. P. (2011). Bulk heterojunction photovoltaic active layers via bilayer interdiffusion. *Nano letters*, *11*(5), 2071-2078.
25. Tang, C. W. (1986). Two-layer organic photovoltaic cell. *Applied Physics Letters*, *48*, 183.
26. Yang, C. Y., &Heeger, A. J. (1996). Morphology of composites of semiconducting polymers mixed with C< sub> 60</sub>. *Synthetic metals*, *83*(2), 85-88.
27. Wienk, M. M., Kroon, J. M., Verhees, W. J., Knol, J., Hummelen, J. C., van Hal, P. A., & Janssen, R. A. (2003). Efficient methano [70] fullerene/MDMO-PPV bulk heterojunction photovoltaic cells. *AngewandteChemie*, *115*(29), 3493-3497.
28. Shaheen, S. E., Brabec, C. J., Sariciftci, N. S., Padinger, F., Fromherz, T., &Hummelen, J. C. (2001). 2.5% efficient organic plastic solar cells. *Applied Physics Letters*, *78*, 841.
29. Hoppe, H., Niggemann, M., Winder, C., Kraut, J., Hiesgen, R., Hinsch, A., ... &Sariciftci, N. S. (2004). Nanoscale Morphology of Conjugated Polymer/Fullerene-Based Bulk-Heterojunction Solar Cells. *Advanced Functional Materials*, *14*(10), 1005-1011.
30. Lim, J. A., Liu, F., Ferdous, S., Muthukumar, M., &Briseno, A. L. (2010). Polymer semiconductor crystals. *Materials Today*, *13*(5), 14-24.

31. Brinkmann, M. (2011). Structure and morphology control in thin films of regioregular poly (3-hexylthiophene). *Journal of Polymer Science Part B: Polymer Physics*, *49*(17), 1218-1233.
32. Sirringhaus, H., Brown, P. J., Friend, R. H., Nielsen, M. M., Bechgaard, K., Langeveld-Voss, B. M. W., ... & De Leeuw, D. M. (1999). Two-dimensional charge transport in self-organized, high-mobility conjugated polymers. *Nature*, *401*(6754), 685-688.
33. Yin, W., & Dadmun, M. (2011). A new model for the morphology of P3HT/PCBM organic photovoltaics from small-angle neutron scattering: rivers and streams. *Acs Nano*, *5*(6), 4756-4768.
34. Hoppe, H., &Sariciftci, N. S. (2004). Organic solar cells: An overview. *Journal of Materials Research*, *19*(07), 1924-1945.
35. Yusli, M. N., Way Yun, T., &Sulaiman, K. (2009). Solvent effect on the thin film formation of polymeric solar cells. *Materials Letters*, *63*(30), 2691-2694.
36. DeLongchamp, D. M., Vogel, B. M., Jung, Y., Gurau, M. C., Richter, C. A., Kirillov, O. A., ... & Lin, E. K. (2005). Variations in semiconducting polymer microstructure and hole mobility with spin-coating speed. *Chemistry of materials*, *17*(23), 5610-5612.
37. Tremolet de Villers, B., Tassone, C. J., Tolbert, S. H., & Schwartz, B. J. (2009). Improving the reproducibility of P3HT: PCBM solar cells by controlling the PCBM/cathode interface. *The Journal of Physical Chemistry C*, *113*(44), 18978-18982.
38. Clarke, T. M.; Ballantyne, A.M.; Nelson, J.; Bradley, D.D.C.; Durrant, J.R. Free Energy Control of Charge Photogeneration in Polythiophene/Fullerene Solar Cells: The Influence of Thermal Annealing on P3HT/PCBM Blends. *Adv. Func. Mater.* **2008**, 18, 24, 4029-4035.
39. Yang, X., Loos, J., Veenstra, S. C., Verhees, W. J., Wienk, M. M., Kroon, J. M., ... & Janssen, R. A. (2005). Nanoscale morphology of high-performance polymer solar cells. *Nano letters*, *5*(4), 579-583.

40. Brédas, J. L., Norton, J. E., Cornil, J., &Coropceanu, V. (2009). Molecular understanding of organic solar cells: the challenges. *Accounts of Chemical Research*, *42*(11), 1691-1699.
41. Zhao, Y., Xie, Z., Qu, Y., Geng, Y., & Wang, L. (2007). Solvent-vapor treatment induced performance enhancement of poly (3-hexylthiophene): methanofullerene bulk-heterojunction photovoltaic cells. *Applied physics letters*, *90*(4), 043504-043504.
42. Park, J. H., Kim, J. S., Lee, J. H., Lee, W. H., & Cho, K. (2009). Effect of annealing solvent solubility on the performance of poly (3-hexylthiophene)/methanofullerene solar cells. *The Journal of Physical Chemistry C*, *113*(40), 17579-17584.
43. Gao, Y.M., T; Grey, J. K, *Understanding Morphology Dependent Polymer Aggregation Properties and Photocurrent Generation in Poly(Thiophene/Fullerene) Solar Cells of Variable Compositions.* J. Phys. Chem., 2010. **2010**(114).
44. Pivrikas, A., Neugebauer, H., &Sariciftci, N. S. (2011). Influence of processing additives to nano-morphology and efficiency of bulk-heterojunction solar cells: A comparative review. *Solar Energy*, *85*(6), 1226-1237.
45. Hähner, G. (2006). Near edge X-ray absorption fine structure spectroscopy as a tool to probe electronic and structural properties of thin organic films and liquids. *Chemical Society Reviews*, *35*(12), 1244-1255.
46. Germack, D. S., Chan, C. K., Kline, R. J., Fischer, D. A., Gundlach, D. J., Toney, M. F., ... &DeLongchamp, D. M. (2010). Interfacial segregation in polymer/fullerene blend films for photovoltaic devices. *Macromolecules*, *43*(8), 3828-3836.
47. Huang, J., Juszkiewicz, M., De Jeu, W. H., Cerda, E., Emrick, T., Menon, N., & Russell, T. P. (2007). Capillary wrinkling of floating thin polymer films. *Science*, *317*(5838), 650-653.

48. Tsoi, W., et al., *The nature of in-plane skeleton Raman modes of P3HT and their correlation to the degree of molecular order in P3HT:PCBM blend thin films.* Journal of the American Chemical Society, 2011. **133**(25): p. 9834-9843.
49. Gao, Y., & Grey, J. K. (2009). Resonance Chemical Imaging of Polythiophene/Fullerene Photovoltaic Thin Films: Mapping Morphology-Dependent Aggregated and Unaggregated C=C Species. *Journal of the American Chemical Society*, *131*(28), 9654-9662.
50. Giridharagopal, R., & Ginger, D. S. (2010). Characterizing morphology in bulk heterojunction organic photovoltaic systems. *The Journal of Physical Chemistry Letters*, *1*(7), 1160-1169.
51. Erb, T., Zhokhavets, U., Gobsch, G., Raleva, S., Stühn, B., Schilinsky, P., ... &Brabec, C. J. (2005). Correlation between structural and optical properties of composite polymer/fullerene films for organic solar cells. *Advanced Functional Materials*, *15*(7), 1193-1196.
52. Chiu, M. Y., Jeng, U., Su, C. H., Liang, K. S., & Wei, K. H. (2008). Simultaneous Use of Small-and Wide-Angle X-ray Techniques to Analyze Nanometerscale Phase Separation in Polymer Heterojunction Solar Cells. *Advanced Materials*, *20*(13), 2573-2578.
53. Li, G., Yao, Y., Yang, H., Shrotriya, V., Yang, G., & Yang, Y. (2007). "Solvent Annealing" Effect in Polymer Solar Cells Based on Poly (3-hexylthiophene) and Methanofullerenes. *Advanced Functional Materials*, *17*(10), 1636-1644.
54. Kline, R. J., McGehee, M. D., Kadnikova, E. N., Liu, J., Frechet, J. M., & Toney, M. F. (2005). Dependence of regioregular poly (3-hexylthiophene) film morphology and field-effect mobility on molecular weight. *Macromolecules*, *38*(8), 3312-3319.
55. Mao-Yuan, C., et al., *Simultaneous Use of Small- and Wide-Angle X-ray Techniques to Analyze Nanometerscale Phase Separation in Polymer Heterojunction Solar Cells.* Advanced Materials, 2008. **20**.

56. Erb, T., et al., *Correlation Between Structural and Optical Properties of Composite Polymer/Fullerene Films for Organic Solar Cells.* Advanced Functional Materials, 2005. **15**.
57. Chen, H., Hegde, R., Browning, J., & Dadmun, M. D. (2012). The miscibility and depth profile of PCBM in P3HT: thermodynamic information to improve organic photovoltaics. *Physical Chemistry Chemical Physics*, *14*(16), 5635-5641.
58. Milojevich, C. B. (2013). Resonance Hyper-Raman Characterization of Nonlinear Chromophores.
59. Wunderlich, B.W., Hans, *Condis Crystals of Small Molecules I. The Concept and Limitations.* Molecular Crystals and Liquid Crystals, 1986. **140**(2-4).
60. DeLongchamp, D. M., Kline, R. J., Fischer, D. A., Richter, L. J., & Toney, M. F. (2011). Molecular characterization of organic electronic films. *Advanced Materials*, *23*(3), 319-337.
61. Liao, H. C., Tsao, C. S., Huang, Y. C., Jao, M. H., Tien, K. Y., Chuang, C. M., ... & Su, W. F. (2014). Insights into solvent vapor annealing on the performance of bulk heterojunction solar cells by a quantitative nanomorphology study. *RSC Advances*, *4*(12), 6246-6253.
62. Quinlan, R. A., Cai, M., Outlaw, R. A., Butler, S. M., Miller, J. R., & Mansour, A. N. (2013). Investigation of defects generated in vertically oriented graphene. *Carbon*, *64*, 92-100.
63. Haiyun, L., A. Bulent, and P.R. Thomas, *Morphological Characterization of a Low-Bandgap Crystalline Polymer:PCBM Bulk Heterojunction Solar Cells.* Advanced Energy Materials, 2011. **1**.
64. G. Li, Y. Yao, H. Yang, V. Shrotriya, G. Yang, Y. Yang, Solvent annealing effect in polymer solar cells based on poly(3-hexylthiophene) and methanofuller- enes, Advanced Functional Materials 17 (2007) 1636–1644.
65. Huang, J., Juszkiewicz, M., De Jeu, W. H., Cerda, E., Emrick, T., Menon, N., & Russell, T. P. (2007). Capillary wrinkling of floating thin polymer films. *Science*, *317*(5838), 650-653.

66. Chung, J. Y., Chastek, T. Q., Fasolka, M. J., Ro, H. W., & Stafford, C. M. (2009). Quantifying residual stress in nanoscale thin polymer films via surface wrinkling. *ACS nano*, *3*(4), 844-852.
67. Stafford, C. M., Harrison, C., Beers, K. L., Karim, A., Amis, E. J., Vanlandingham, M. R., ... & Simonyi, E. E. (2004). A buckling-based metrology for measuring the elastic moduli of polymeric thin films. *Nature materials*, *3*(8), 545-550.
68. Davidovitch, B., Schroll, R. D., Vella, D., Adda-Bedia, M., &Cerda, E. A. (2011). Prototypical model for tensional wrinkling in thin sheets. *Proceedings of the National Academy of Sciences*, *108*(45), 18227-18232.
69. Yasuda, H., &Rosengren, K. J. (1970). Isobaric measurement of gas permeability of polymers. *Journal of Applied Polymer Science*, *14*(11), 2839-2877.
70. George, S. C., & Thomas, S. (2001). Transport phenomena through polymeric systems. *Progress in Polymer Science*, *26*(6), 985-1017.
71. Haraya, K., & Hwang, S. T. (1992). Permeation of oxygen, argon and nitrogen through polymer membranes. *Journal of membrane science*, *71*(1), 13-27.Ghosal, K., & Freeman, B. D. (1994). Gas separation using polymer membranes: an overview. *Polymers for advanced technologies*, *5*(11), 673-697.
72. Ghosal, K., & Freeman, B. D. (1994). Gas separation using polymer membranes: an overview. *Polymers for advanced technologies*, *5*(11), 673-697.
73. Kawakami, Y., Aoki, T., & Yamashita, Y. (1986). Enhanced Oxygen Permeation through Surface Modified Blend Films Containing Polydimethylsiloxane Graft Copolymers.

APPENDIX

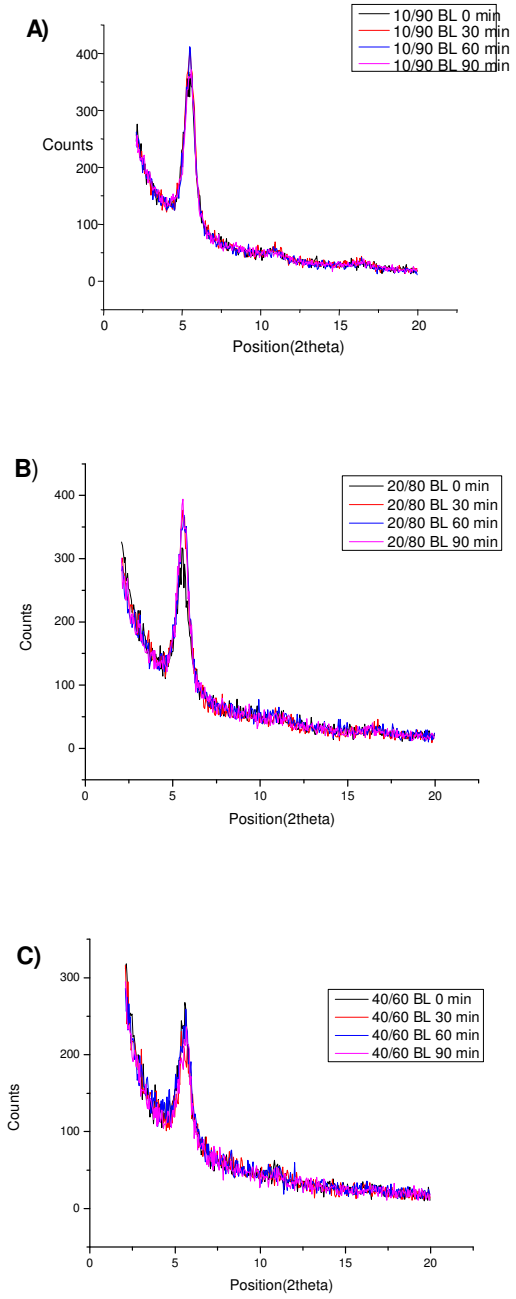

Figure 2.4.1: GIXRD spectra of A) 10/90 PCBM:P3HT Bilayer B) 20/80 PCBM:P3HT bilayer C) 40/60 PCBM:P3HT bilayer. All three systems were solvent annealed in ODCB at 90 percent SVP for 30,60, and 90 minutes.

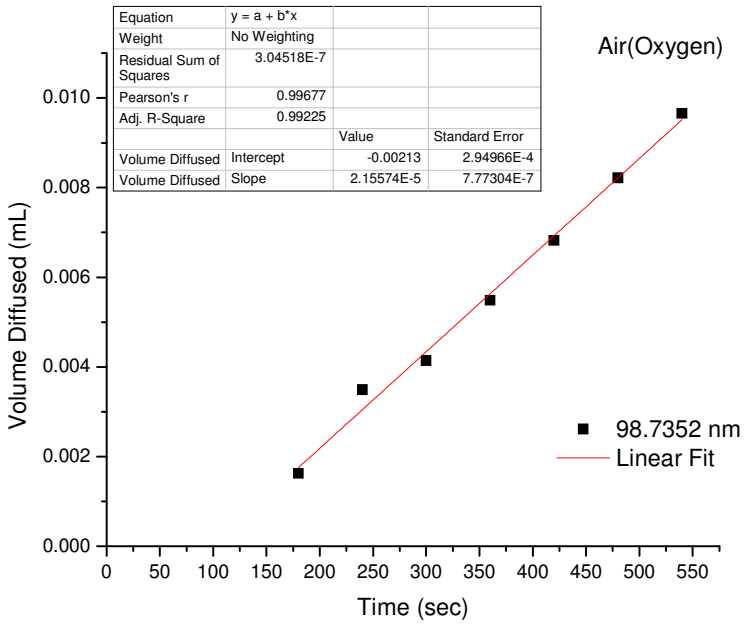

Figure 1A: Linear fit of volume of oxygen in air diffused as a function of time.

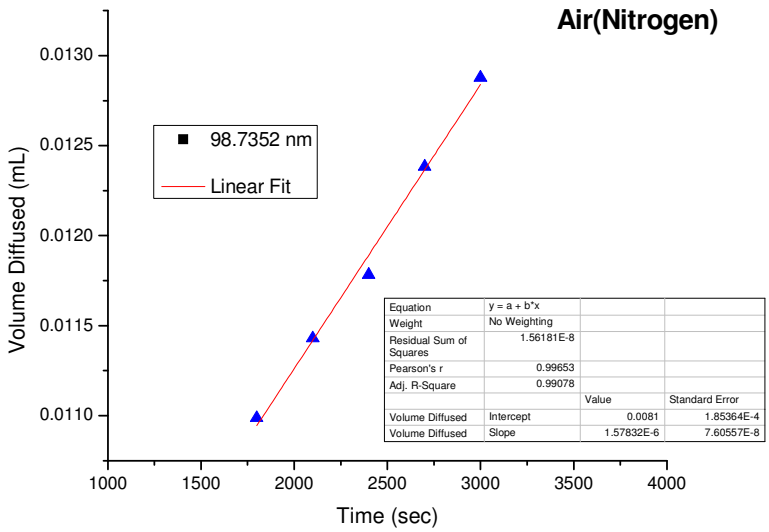

Figure 2A: Linear Fit of change in the volume of nitrogen in air as a function of time.

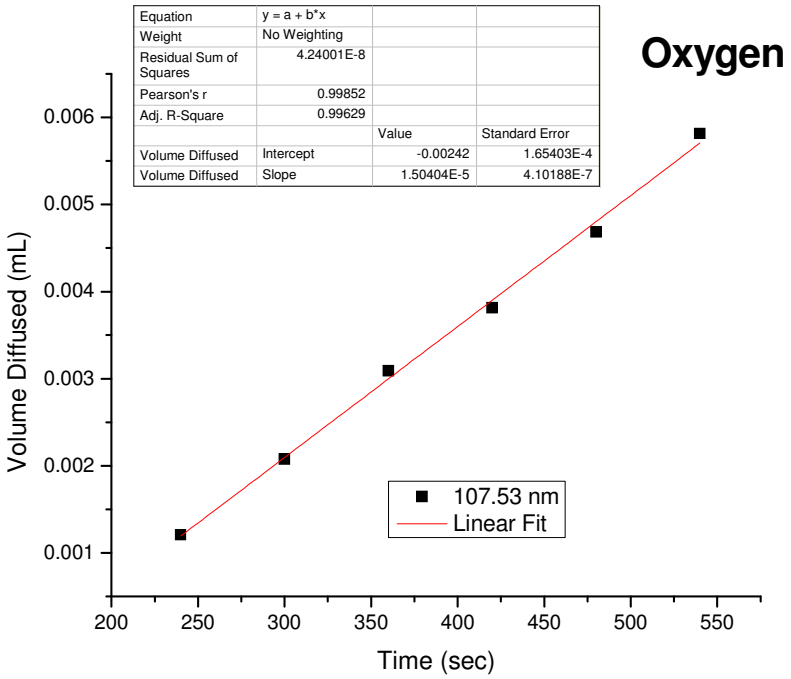

Figure 3A: Linear fit of change in the volume of pure oxygen as a function of time

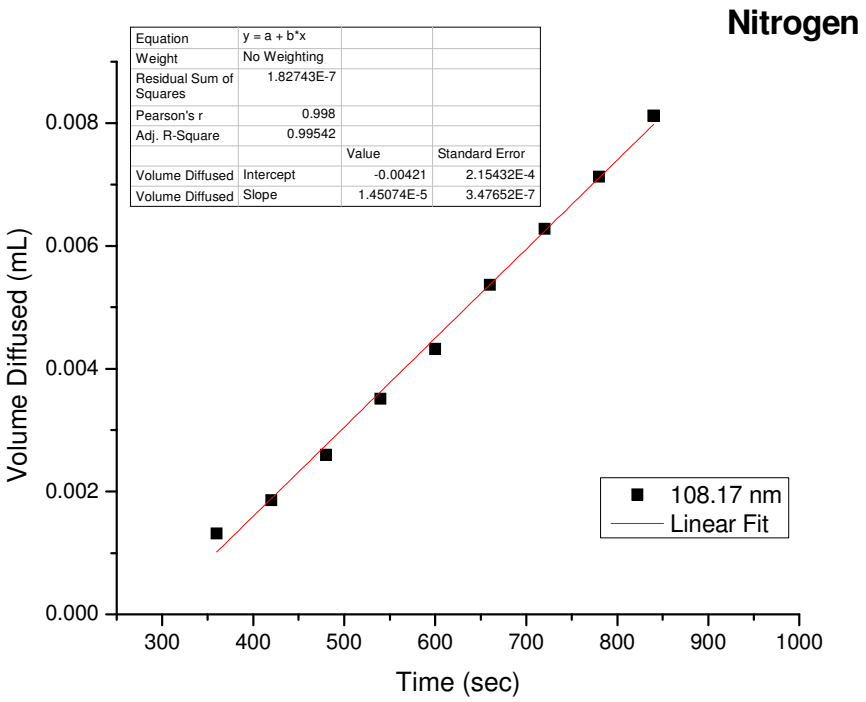

Figure 4A: Linear fit of volume change of pure nitrogen through 108.17 nm polystyrene film.

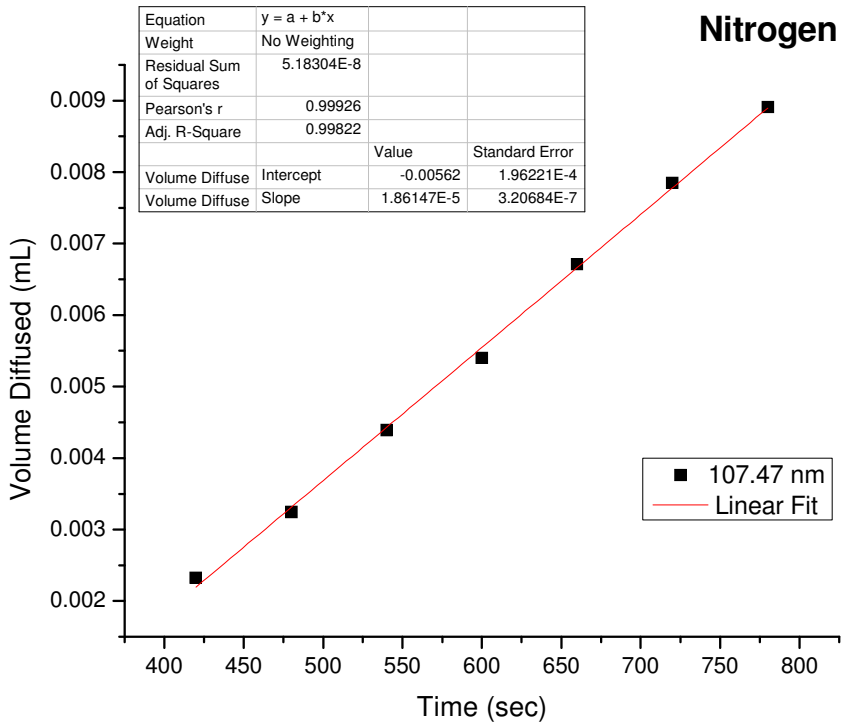

Figure 5A: Linear fit of volume change of pure nitrogen through a 107.47 nm polystyrene film.

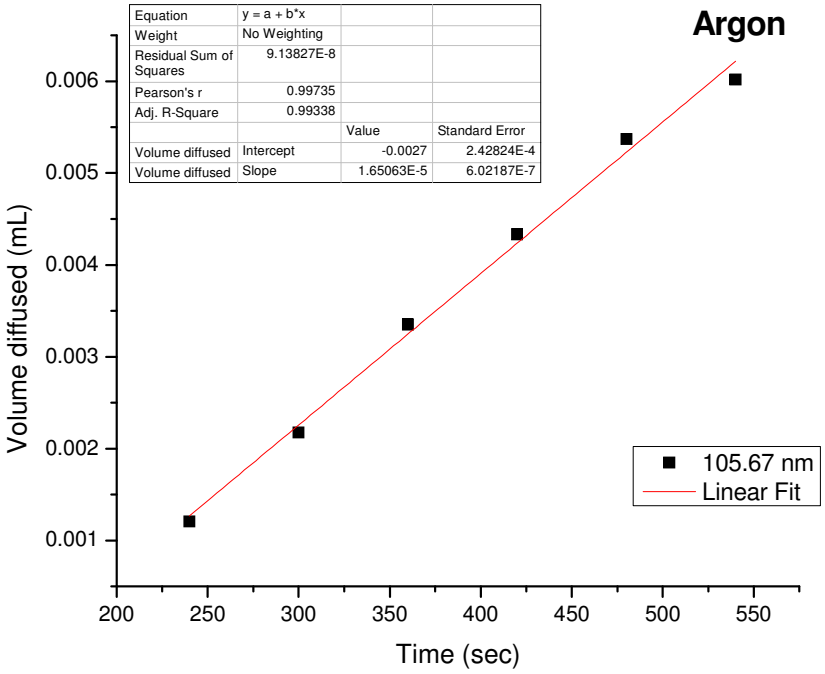

Figure 6A: Volume change of argon gas as a function of time. A linear fit was used to calculate the x intercept (time lag θ).

VITA

Tyler McPherson was born in Monroeville, AL to the parents of Randal and Kathy McPherson. He graduated from Excel High School in May 2006. He attended Alabama Southern Community College from June 2006 to May 2008 where he was awarded an Associates in Science with honors degree. He received a transfer scholarship to attend the University of Alabama, Tuscaloosa. While attending, he was a member of the Million Dollar Band and Gamma Sigma Epsilon Chemistry Honor Society. He worked as an undergraduate researcher in Dr. Shanlin Pan's lab. He also participated in summer REU programs at Auburn University, University of South Alabama, and the University of Alabama. He graduated in December 2010 with a Bachelors of Science in Chemistry (ACS certified). He received a graduate teaching/research scholarship to attend the University of Tennessee, Knoxville in August 2011. He joined the research group of Dr. Mark Dadmun working on characterizing the morphology of solvent annealed organic photovoltaics. He graduated from Tennessee in May 2014 with a Master of Science Degree in Polymer Chemistry. He is currently employed as a research and development engineering at Toray Carbon Fibers in Decatur, AL.